Analysis Note for $\gamma p \to p\phi\eta$

Bradford E. Cannon

October 2, 2018

Table of Contents

1 Selecting $\gamma p \to p\phi\eta$ Events at GlueX

In order to study potential states of bound strangeonia, it is essential to properly identify all final and initial state particles. The final state topology that will be studied for this thesis is $\gamma p \to p K^+ K^- \gamma_1 \gamma_2$, where the $K^+ K^-$ pair are daughter states of the ϕ meson, and the $\gamma_1 \gamma_2$ pair are daughter states of the η meson. Therefore, the beginning of this analysis section will focus on the particle identification of the proton, kaons, and final state photons, as well as the incident beam and target proton. Once identification of all particles has been well established, this analysis will then investigate whether or not a correlation exists between the ϕ and η bound states. This analysis will be conducted by means of sampling different regions of the $\gamma_1 \gamma_2$ invariant mass and the $K^+ K^-$ invariant mass. Ultimately, it will be shown that a correlation does in fact manifest itself within this data set, and therefore a thorough strangeonia analysis can be performed.

1.1 Spring 2017 Run Period

The data presented here is the result of the successful Spring 2017 Low Intensity run period. The Spring 2017 run period spanned from January 23rd to March 13th and accumulated roughly 50 billion physics events. The maximum electron beam energy used was 12 GeV, and the accelerator ran at 250 MHz while in low intensity (beam every 4 ns), and later ran at 500 MHz while in high intensity (beam every 2 ns). Upon entering Hall D, the electron beam was incident upon a radiator. During this run period, both amorphous and diamond radiators were used to produce either incoherent or coherent polarized bremsstrahlung radiation. The diamond radiator was experimentally set up to produce linear photon polarization at four different angles; 0°, 45°, 90°, and 135°. These directions were chosen in order to provide the detector with a uniform sampling of linear polarization in the transverse direction to the incident beam. In order to yield roughly the same amount of statistics for an amorphous radiator run as compared to a diamond radiator run, a beam current of 150 nA was incident upon the amorphous radiator, while a beam current of 100 nA was incident upon the diamond radiator. Farther downstream, a 5mm collimator hole was used for all radiator configurations. Lastly, the collimated photon beam was incident upon a stationary liquid hydrogen target. This resulted in one petabyte of files and $16pb^{-1}$ of integrated luminosity.

2

1.2 Particle Identification

Once all of the data files were written to disk, an analysis launch was initiated. Part of this analysis launch searched for the $\gamma p \to pK^+K^-\gamma\gamma$ topology and incorporated a kinematic fitter which simultaneously constrained four momentum and a common production vertex for the final state particles. It should be noted that this analysis did not enforce the K^+K^- pair come from a ϕ parent state, or the $\gamma\gamma$ pair come from an η parent state; even though the ultimate goal of this analysis is to study the parent states of $\phi\eta$. After successful completion of the analysis launch, the data was then processed by a DSelector which applied several cuts to the data. Initial cuts on the data included timing cuts in the Barrel Calorimeter (BCAL), Forward Calorimeter (FCAL), and the Time of Flight detector (TOF). These timing cuts were made for all of the final state particles $(p, K^+, K^-, \gamma_1, \gamma_2)$. A table of the timing cuts used for each final state particle and its associated detector apparatus is given in Table 1. An in depth explanation of these cut values and how they were chosen is provided in the subsection 3.2.

A list of timing plots for all of the final state particles and detector systems is given in Figures 1234. In these Figures, the top plot includes timing measurements from the BCAL, the middle plot includes timing measurements from the FCAL, and the bottom plot includes timing measurements from the TOF. All plots have the timing on the vertical axis and the measured magnitude of the three momentum on the horizontal axis. The 'z' axis is logarithmically scaled with the relative values given by the color bar to the of the plots. The ΔT measurement comes from comparing the measured timing from the associated detector with the time reported by the RF, or beam. To identify particles, we want to only select candidates that have a ΔT close to zero.

After the timing cuts for all of the final state particles was performed, additional cuts were made to identify the $\gamma p \to pK^+K^-\gamma_1\gamma_2$ final state. One of these cuts included enforcing the reconstructed vertex for all final state particles to be within the geometric volume of the target chamber. Since this analysis does not contain a particle lifetime which would result in a detached vertex, it is imperative to remove backgrounds from other channels that may have this feature, such as excited baryons with a strange quark. An example of what the reconstructed vertex for the final state photons looks like in the z direction (along the beam direction) and in the x-y plane (transverse to the beam direction), as well as the associated cut values, is given in Figure 5.

Another additional cut that is made on the data pertains directly to the identification of the correct beam photon bunch. Since the electron beam is delivered from the accelerator every four nanoseconds, the timing of when

Particle	Detector	ΔT Cut [ns] (2σ)
Proton	BCAL	$\pm\ 0.6$
Proton	FCAL	$\pm\ 1.0$
Proton	TOF	$\pm\ 0.4$
K^+	BCAL	$\pm\ 0.7$
K^+	FCAL	$\pm\ 0.8$
K^+	TOF	$\pm\ 0.2$
K^-	BCAL	$\pm\ 0.7$
K^-	FCAL	$\pm\ 0.8$
K^-	TOF	$\pm\ 0.2$
γ	BCAL	$\pm\ 1.0$
γ	FCAL	$\pm\ 1.1$

Table 1: A table with timing cut values for all final state particles in the reaction $\gamma p \rightarrow p K^+ K^- \gamma_1 \gamma_2$. The values of the timing cuts change depending on both the particle species and detector system resolution. It should be noted that the final state photons only have the calorimeters as possible timing detectors. This is due to the fact that they do not interact with the TOF detector.

the particles arrive into the hall is well known and we call the the Radio Frequency (RF) time. However, once the photons are in the hall, it is unclear which beam bunch may have caused the subsequent physics event. When a physics event takes place, there is an associated beam time which is recoded by either the tagger hodoscope or the tagger microscope. This device can measure both the energy of the beam and the timing of the beam. One of the cuts is made on the the data presented is the difference between the recorded beam time and the reported RF time. An example of what this data looks like and the cut used for it is given in Figure 6.

The last cut that was performed by the DSelector was the value of the observed beam energy. Although this cut does not technically fall under the category of a particle identification, it is included in this section because it was used as a prerequisite for the rest of this analysis. Since this study will ultimately focus on a reaction which requires a high 't' momentum transfer, it is natural to only allow beam photons with high momentum to begin with. This, coupled with the fact that low energy photons produce low statistics for this channel, is the reason why a beam energy cut of $Beam_E \geq 7.5$ GeV was enforced early in the analysis. It should also be noted that this analysis will include a beam asymmetry study for strangeonia which will force the beam energy to be within the coherent peak region ($8.0 GeV - 8.8 GeV$).

An example beam energy distribution with the associated cut is given in Figure 7.

1.3   Kinematic Fit Confidence Level Cut Study

This is where I am... Need to continue editing document from here...The first of the cuts included a kinematic fit confidence level cut of $1x10^{-4}$. This kinematic fit confidence level was chosen based on a study that was performed on this data after it was processed by the analysis launch. In this study, both the η and ϕ peaks from the $\gamma\gamma$ and K^+K^- invariant mass spectra were fitted as a function of kinematic fit confidence level cut. The η peak was fitted with a Gaussian plus a first degree polynomial while the ϕ peak was fitted with a Gaussian plus a second degree polynomial. Examples of an η fit from this study is given in Figure 8, and an example ϕ fit from this study is given in Figure 9. In each figure, the blue line represents the sum of the Gaussian plus the polynomial fits, the green line represents the Gaussian fit, and the red line represents the polynomial fit. Additionally, both figures are the result of a kinematic fit confidence level cut of $1x10^{-4}$. It should be noted that the mean values and widths obtained from these Gaussian fits will serve as the observed massed and widths for the rest of this analysis. More specifically, the mass and width for the η was found to be $m_\eta = 0.545, \sigma_\eta = 0.02883$ (GeV/c^2); and the ϕ mass and width was found to be $m_\phi = 1.02, \sigma_\phi = 0.005917$ (GeV/c^2). Due to the high amount of statistics associated with this topology at this point, it was only necessary to include fifteen files to perform this study.

After the fits for the ϕ and η peaks were performed at different confidence levels, an integration of the Gaussian function and polynomial function was calculated. The results of these integrations plotted as a function of kinematic fit confidence level provides an indication of where an appropriate confidence level cut should be for this analysis. The outcomes of these integrations are provided in Figure 10 for the η meson and also in Figure 11 for the ϕ meson. Both figures contain a red and green line where the red line is the integrated value for the background polynomial and the green line is the integrated value for the Gaussian fit. Each plot contains ten points, denoted with a + symbol, which represent the values obtained at different kinematic fit confidence level values. One can easily observe that for both the ϕ and η plots, the integration of background events drops substantially as the kinematic fit confidence level cut becomes tighter. Additionally, the integration of signal events stays relatively flat as a function of cut value, an indication that the kinematic fitter is performing correctly. Ultimately, the value of $1x10^{-4}$ was chosen as the final kinematic fit cut value since it removed a large amount of background events for both the ϕ and η, while
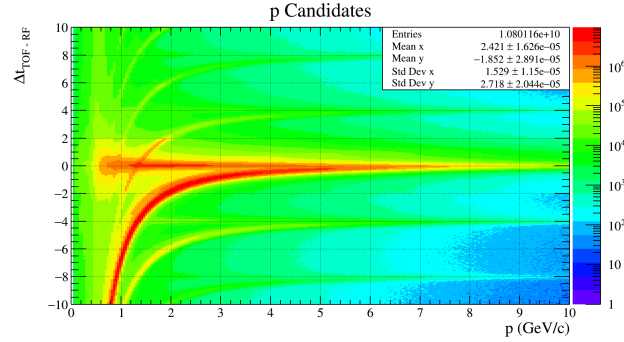
also preserving an appropriate amount of signal events.
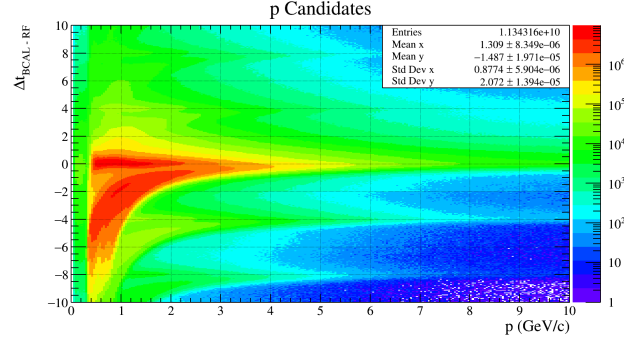
(a) Δ T Vs P for Proton candidates that have the Barrel Calorimeter as the timing detector.
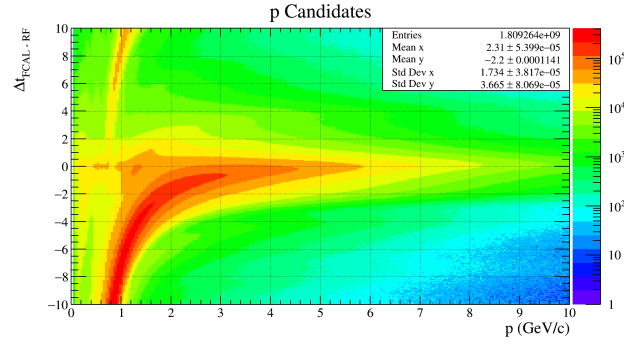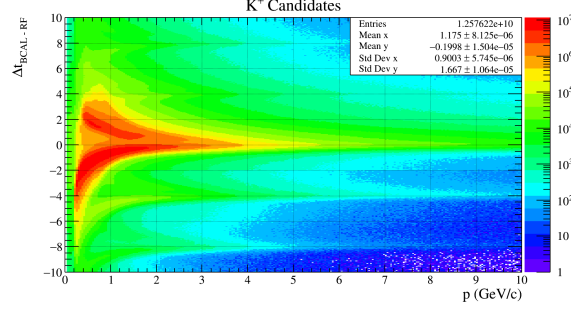

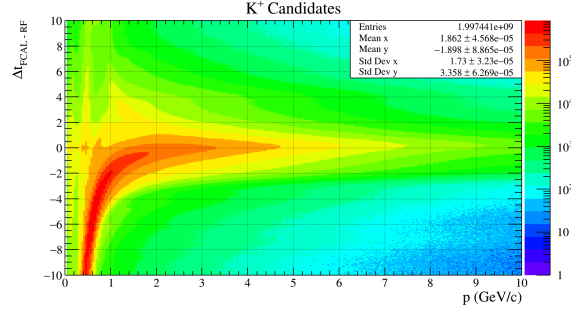(b) Δ T Vs P for Proton candidates that have the Forward Calorimeter as the timing detector.

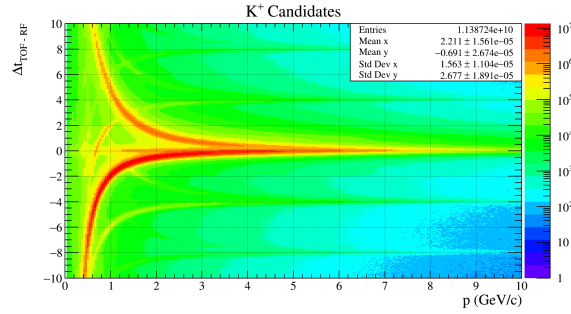(c) Δ T Vs P for Proton candidates that have the Time of Flight as the timing detector.

Figure 1: Timing plots for proton candidates at GlueX. Protons are identified by selecting the horizontal band centered about $\Delta T = 0$. The curved line deviating below the horizontal proton line comes from miss identified π^+ tracks. The additional curved lines above and below $\Delta T = 0$ come from π^+ tracks that are associated with the wrong RF bunch.

(a) Δ T Vs P for K^+ candidates that have the Barrel Calorimeter as the timing detector.

(b) Δ T Vs P for K^+ candidates that have the Forward Calorimeter as the timing detector.

(c) Δ T Vs P for K^+ candidates that have the Time of Flight as the timing detector.

Figure 2: Timing plots for K^+ candidates at GlueX. K^+ are identified by selecting the horizontal band centered about $\Delta T = 0$. The curved line deviating below the horizontal K^+ line comes from miss identified π^+ tracks, and the curved line deviating above the horizontal K^+ line comes from miss identified proton tracks. The additional curved lines above and below $\Delta T = 0$ come from π^+ and proton tracks that are associated with the wrong RF bunch.

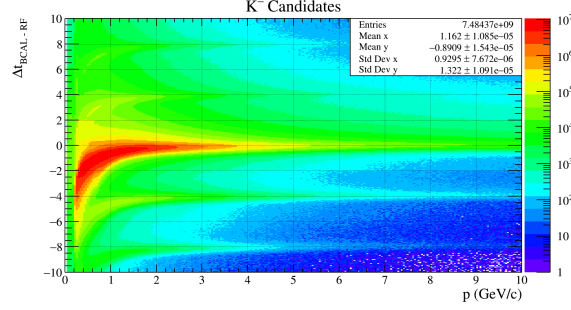(a) Δ T Vs P for K^- candidates that have the Barrel Calorimeter as the timing detector.

(b) Δ T Vs P for K^- candidates that have the Forward Calorimeter as the timing detector.
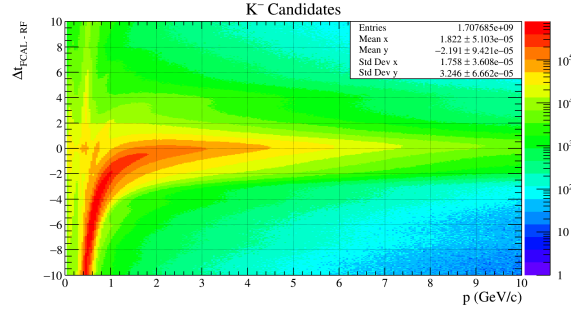

(c) Δ T Vs P for K^- candidates that have the Time of Flight as the timing detector.
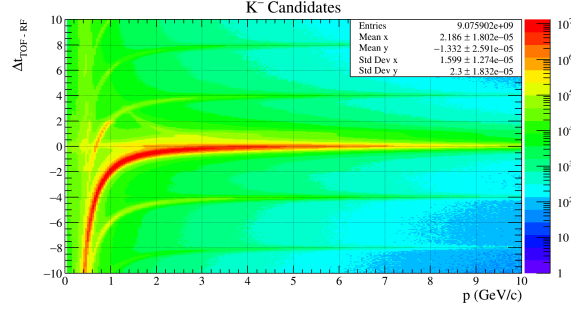
Figure 3: Timing plots for K^- candidates at GlueX. K^- are identified by selecting the horizontal band centered about $\Delta T = 0$. The curved line deviating below the horizontal K^- line comes from miss identified π^- tracks. The additional curved lines above and below $\Delta T = 0$ come from π^- tracks that are associated with the wrong RF bunch.

9

(a) Δ T Vs Shower Energy for γ candidates that have the Barrel Calorimeter as the timing detector.
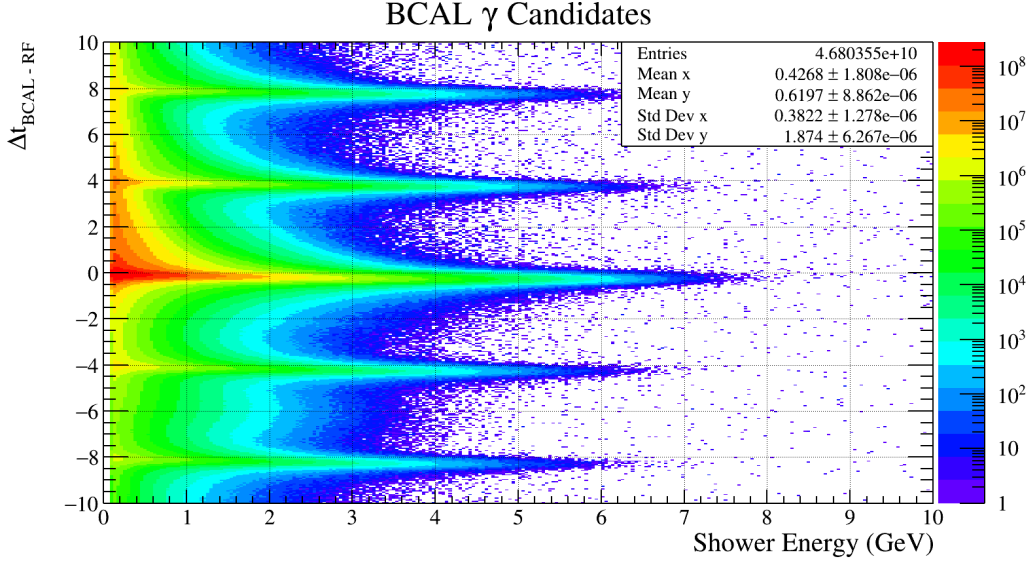

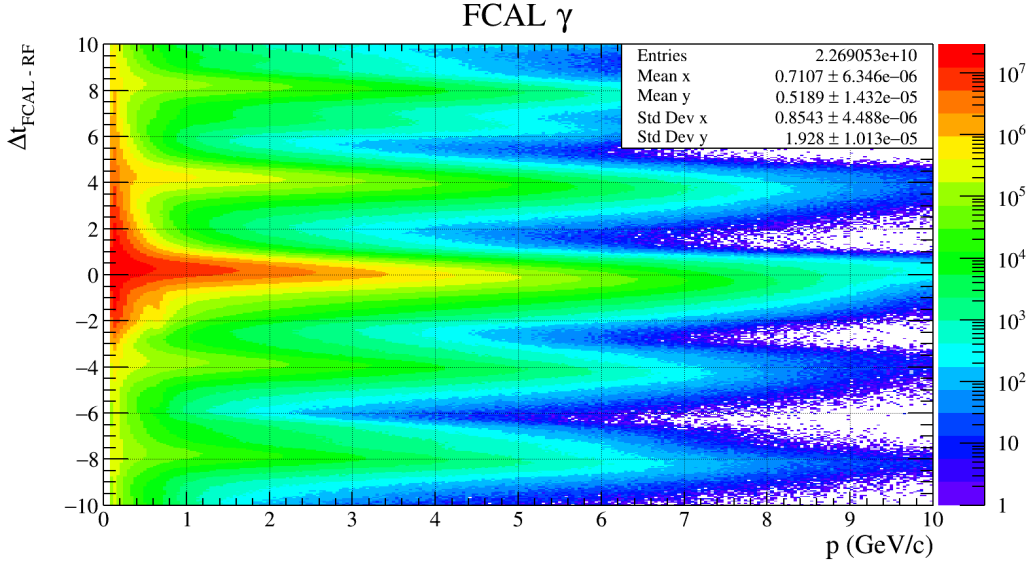(b) Δ T Vs Shower Energy for γ candidates that have the Forward Calorimeter as the timing detector.

Figure 4: Timing plots for γ candidates at GlueX. γ are identified by selecting the horizontal band centered about $\Delta T = 0$. Large enhancement in statistics at low momentum and out of time with the γ line comes from slow moving and poorly times neutrons. The additional horizontal lines above and below $\Delta T = 0$ come from γ showers that are associated with the wrong RF bunch.
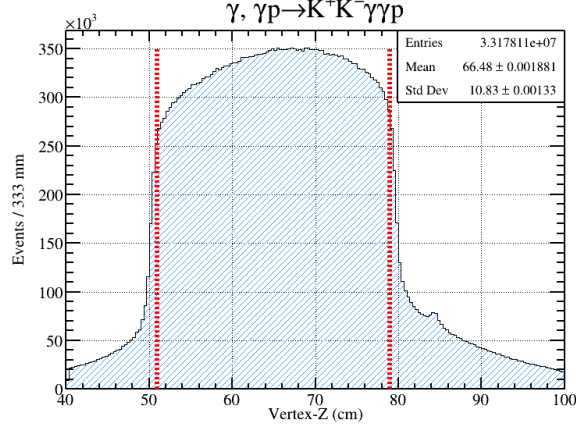
(a) Reconstructed vertex position along the beam direction for γ gamma candidates with cut lines at 51 and 79 cm.
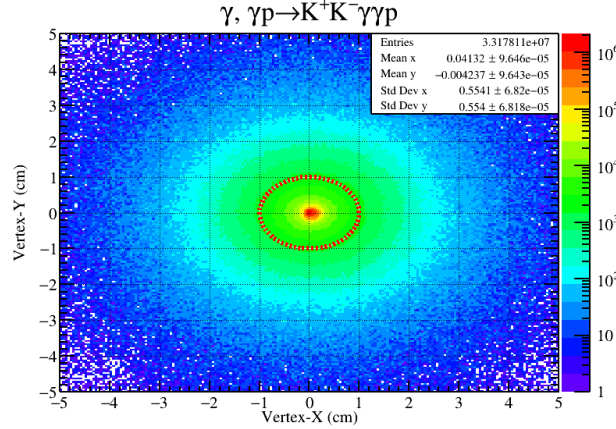
(b) Reconstructed vertex position transverse to the the beam direction for γ gamma candidates with cut a line at 1 cm in radial distance.

Figure 5: An example of what a reconstructed vertex distribution looks like for a final state γ in the reaction $\gamma p \rightarrow pK^+K^-\gamma_1\gamma_2$. The upper image is the reconstructed vertex position along the beam line, or z axis; and the lower image is the reconstructed vertex position in the directions transverse to the beam line. Both figures contain red dashed lines which represent the cut values for all reconstructed final state particles. In the z direction the cut values are $51cm \leq V_z \leq 79cm$, and in the transverse direction the cut values are $V_r \leq 1cm$. The z direction cut values are established from Log Entry 3456336 from a Spring 2017 empty target run. The transverse cuts are simply established by considering the geometric size of the target chamber.
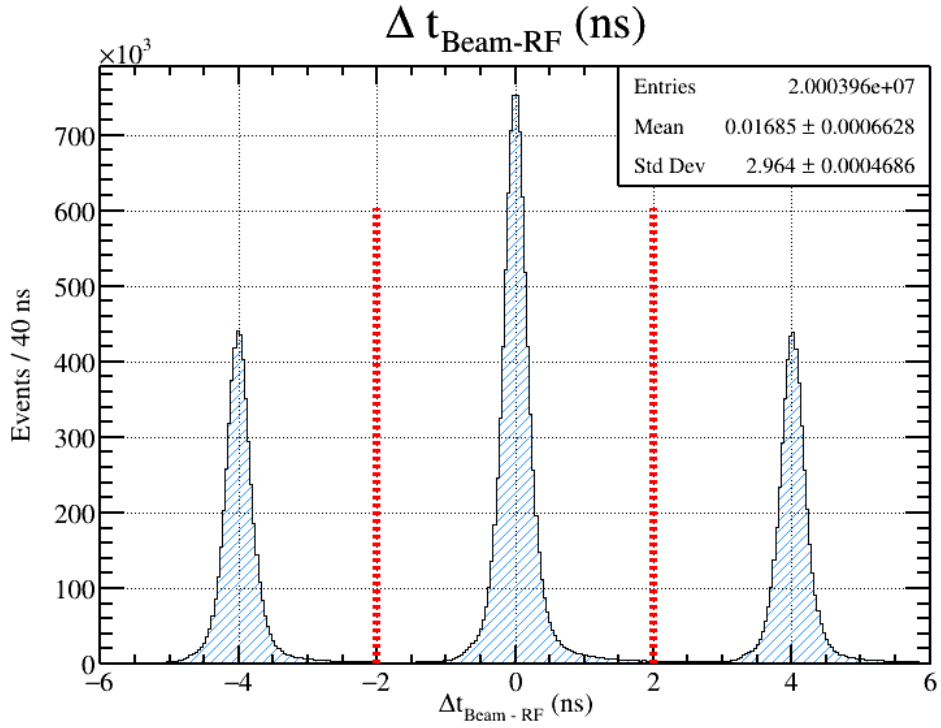
Figure 6: An example histogram of beam time as compared to the reported Radio Frequency (RF) time. In the plot there are three peaks, all of which are separated by four nanoseconds. Also included in the plot are two red dashed cut lines at ± 2 ns. These cut lines will select the beam time which agrees with the RF and will reject the other out of time beam particles.
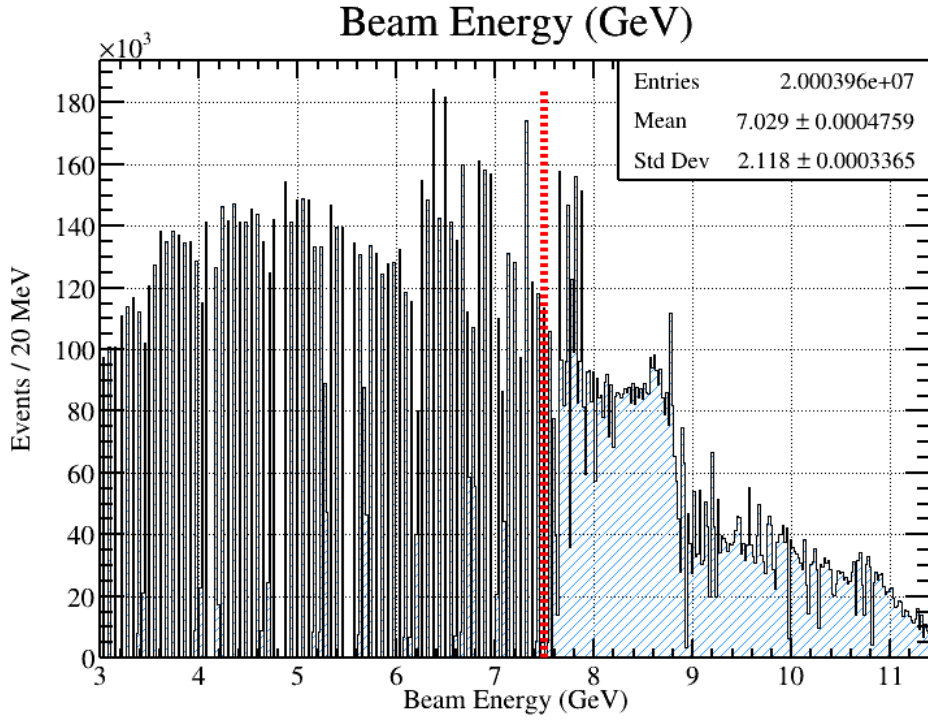
Figure 7: An example histogram of the beam energy distribution at GlueX. One can easily notice the large amount of statistics present around the coherent peak region ($8.0GeV - 8.8GeV$) and energies above it. Also contained in the image is a red dashed line which represents the cut value used on this data to select beam energies above 7.5 GeV.
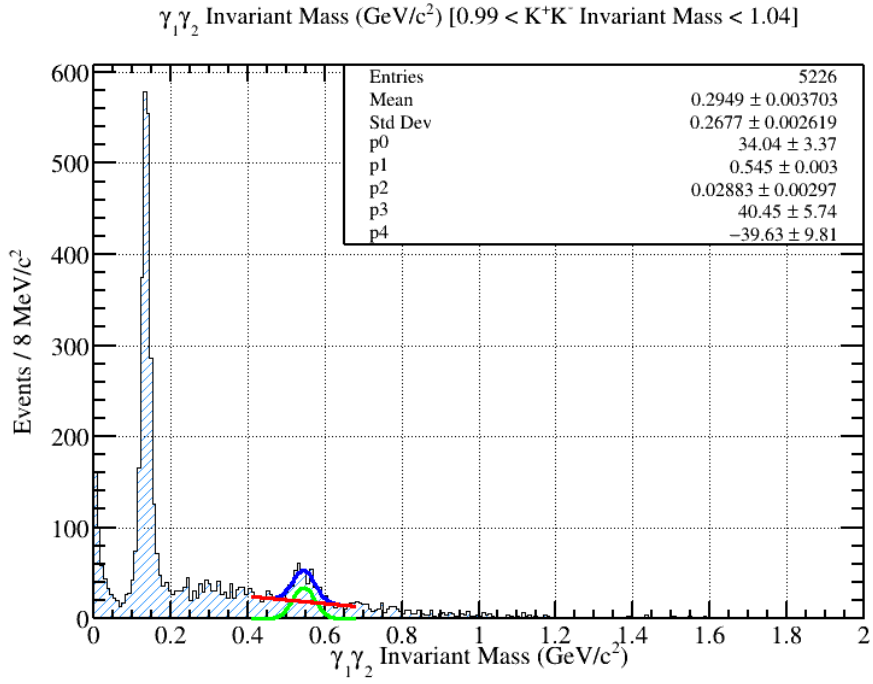
Figure 8: The $\gamma_1\gamma_2$ invariant mass obtained after a kinematic fit confidence level cut of $1x10^{-4}$ and requiring the K^+K^- invariant mass be between the values of 0.99 and 1.04 GeV/c^2 in order to reduce redundant backgrounds. The spectra shows clear π^0 and η peaks at appropriate mass value. The figure also includes three fits where the blue line represents a Gaussian plus a first degree polynomial, the green line represents the Gaussian fit, and the red line represents the first degree polynomial. The constants associated with these fits are listed in the legend.

14
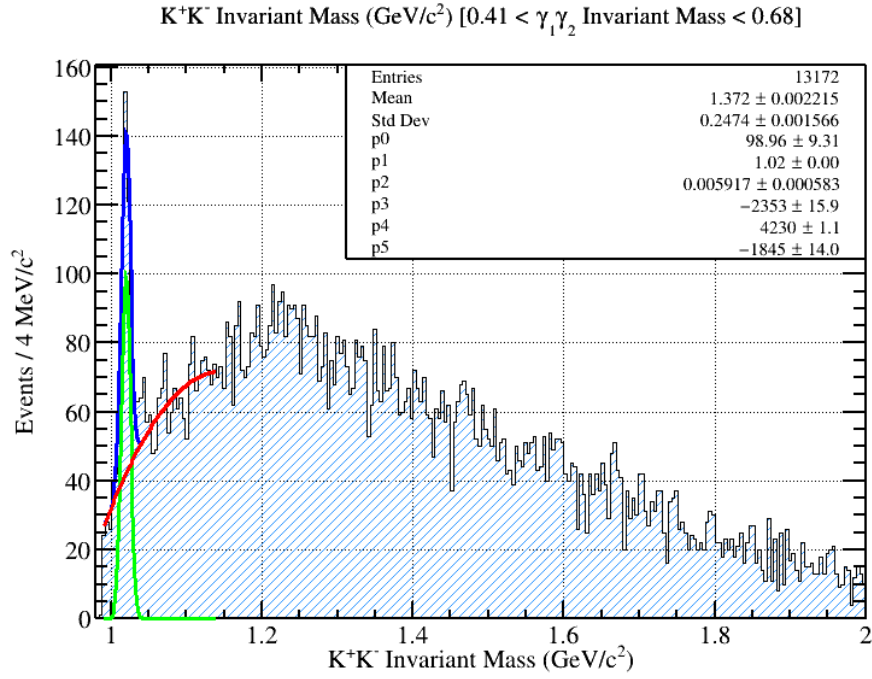
Figure 9: The K^+K^- invariant mass obtained after a kinematic fit confidence level cut of $1x10^{-4}$ and requiring the $\gamma_1\gamma_2$ invariant mass be between the values of 0.41 and 0.68 GeV/c^2 in order to reduce redundant backgrounds. The spectra shows a clear ϕ peak with a minimal amount of background. The figure also includes three fits where the blue line represents a Gaussian plus a second degree polynomial, the green line represents the Gaussian fit, and the red line represents the second degree polynomial. The constants associated with these fits are listed in the legend.

15
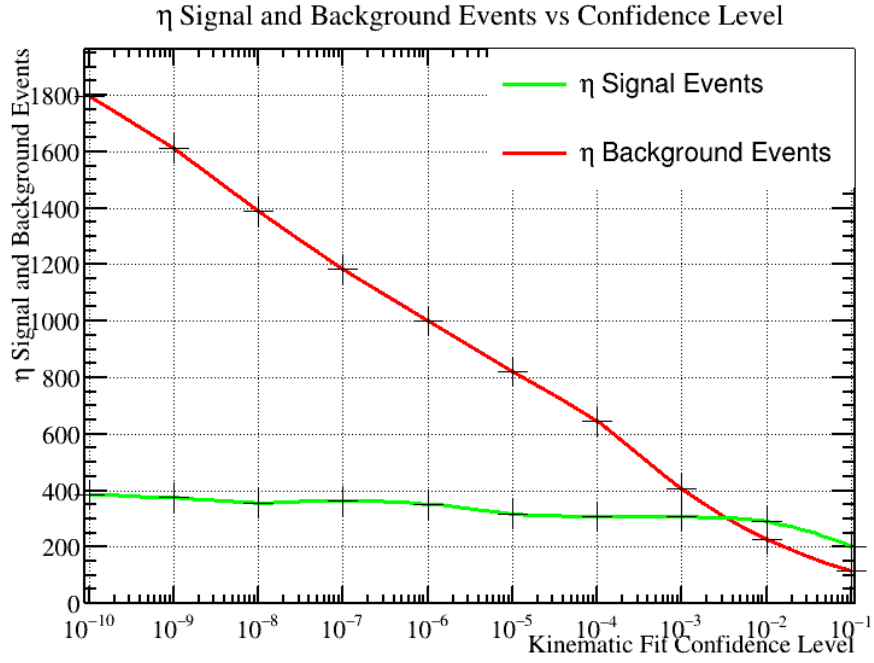
Figure 10: A graph of the η signal and background events as a function of the kinematic fit confidence level cut. The graph contains a red line which represents the integrated η background events from a first order polynomial, and a green line which represents the integrated η signal events from a Gaussian fit function. The graph indicates that the kinematic fitter is working appropriately such that the total number of background events falls as the kinematic fit confidence level cut is increased. Additionally, the total number of signal events stays relatively flat. This graph helps to provide an appropriate kinematic fit cut value that will be used for the rest of this analysis.
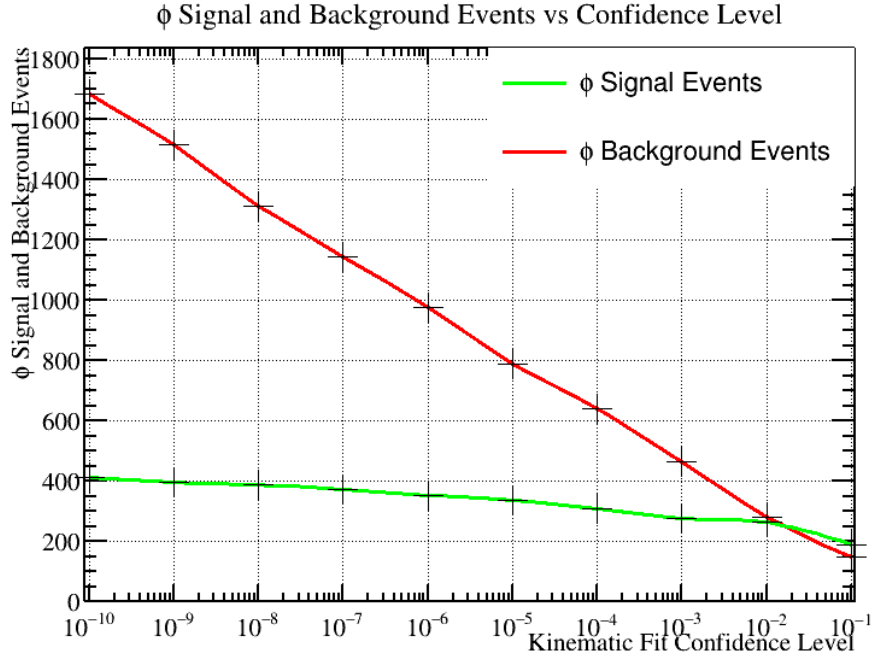
Figure 11: A graph of the ϕ signal and background events as a function of the kinematic fit confidence level cut. The graph contains a red line which represents the integrated ϕ background events from a second order polynomial, and a green line which represents the integrated ϕ signal events from a Gaussian fit function. Just like the η graph before it in Figure 8, the total number of background events falls as the kinematic fit confidence level cut is increased and the total number of signal events stays relatively flat.

2 Investigation of $\phi\eta$ correlation by means of K^+K^- Vs $\gamma_1\gamma_2$ Invariant Mass Plot

The image illustrated in Figure 12 is the data in question. On the vertical axis is the K^+K^- invariant mass and on the horizontal axis is the $\gamma_1\gamma_2$ invariant mass. To be absolutely clear, this is a plot of invariant mass versus invariant mass and is therefore not a Dalitz Plot. Some interesting features contained within the image are the clear vertical bands for the π^0 and η resonances which have large decay modes to $\gamma\gamma$ final states. In addition, one can also observe a horizontal band slightly above 1 $\frac{GeV}{c^2}$ which corresponds to the ϕ meson decaying to a K^+K^- final state. This analysis will focus on the region where the ϕ meson and η meson bands cross in order to determine if their intersection region contains some type of correlation.
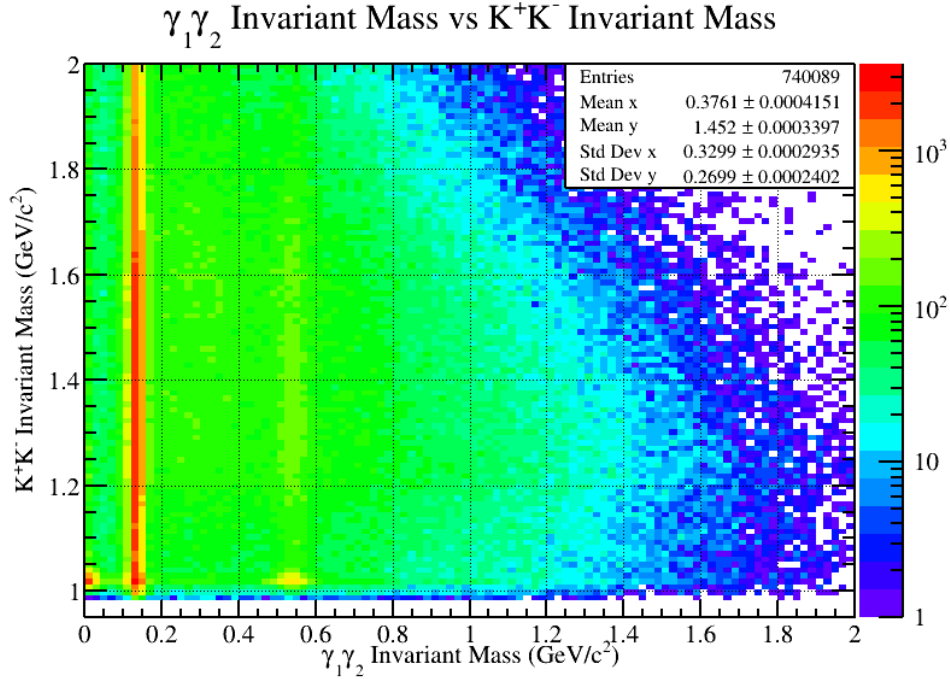
Figure 12: A two dimensional invariant mass plot with the K^+K^- invariant mass on the vertical axis, the $\gamma_1\gamma_2$ invariant mass on the horizontal axis, and a logarithmically scaled z axis. Some interesting features contained within the image are the clear vertical bands for the π^0 and η resonances which have large decay modes to $\gamma\gamma$ final states. In addition, one can also observe a horizontal band slightly above 1 $\frac{GeV}{c^2}$ which corresponds to the ϕ meson decaying to a K^+K^- final state.

2.1 Cuts on the 2D Invariant Mass Plot

In order to analyze the $\phi\eta$ region of this data, only events which fall within $\pm 10\sigma_\phi$ away from the ϕ peak and $\pm 10\sigma_\eta$ away from the η peak will be considered. This was done by taking different slices of either the $\gamma\gamma$ or K^+K^- data, then projecting the invariant mass distribution onto the opposite axis. For example, there were five different ϕ mass regions studied in this analysis. Each fit corresponds to a different $\gamma\gamma$ mass range. The $\gamma\gamma$ mass ranges are all $4\sigma_\eta$ in width, and span a total mass range of $m_\eta - 10\sigma$ to $m_\eta + 10\sigma$. An illustrated example with labeled cut lines is provided in Figure 13. It should be noted that the analysis of the η mass was not studied symmetrically about the ϕ due to the fact that going more than $m_\phi - 6\sigma_\phi$ away from the ϕ peak would result in no events because of the K^+K^- threshold.
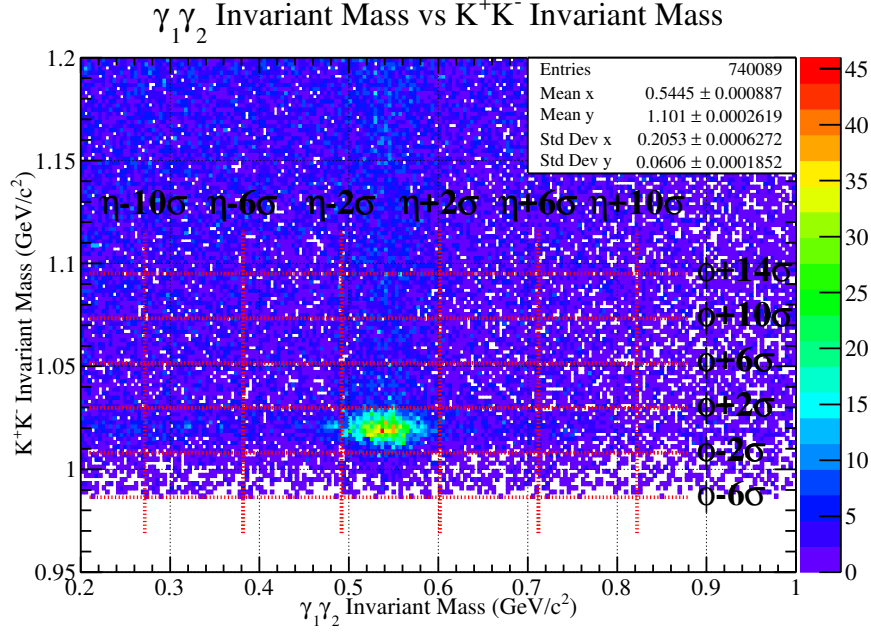
Figure 13: An illustrated example of the cuts used for studying the correlation of $\phi\eta$. The figure above is a two dimensional invariant mass plot which clearly shows an η band spanning the vertical direction at $\sim 0.547 GeV/c^2$ and a ϕ band spanning the horizontal direction at $\sim 1.02 GeV/c^2$. The red vertical and horizontal cut lines provide the ranges used to study $\phi\eta$ correlation. Examples of what the projected ranges look like are provided in Figures [14][15].

19

2.2 Projections and Fits for ϕ and η

Once the data had been cut and projected in the ten different mass regions, the ϕ and η peaks were fit. In the instance of the ϕ meson, the signal plus background events were fit with a Gaussian plus a second degree polynomial. The fit range used in each histogram projection for the ϕ meson spans from $m_\phi - 6\sigma_\phi$ to $m_\phi + 30\sigma_\phi \frac{GeV}{c^2}$. The unusually large fit range was necessary in order to properly estimate the background surrounding the ϕ mass. In the instance of the η meson, the signal plus background events were fit with a Gaussian plus a first degree polynomial due to the relatively flat background surrounding the η peak. The fit range used for the η meson spans $m_\eta \pm 6\sigma_\eta \frac{GeV}{c^2}$. The resulting fits are provided in the images below where the blue line represents the fit for all events (signal plus background), the green line represents the Gaussian fit (signal events), and the red line represents the polynomial fit (background events). Each histogram contains a title with brackets at the end. The arguments encapsulated by the brackets is the cut range that was used for that particular projection sample.

2.3 Integration Results for ϕ and η

After obtaining accurate fits for all regions, integration of the Gaussian fit functions was performed. Each Gaussian fit was integrated in the range of $m \pm 2\sigma_m$, where m represents either m_ϕ or m_η mass coupled with the addition or subtraction of two standard deviations in each direction. Integration of the Gaussian fits provides an accurate estimate for the number of signal events that exists for that particular sampling of $\gamma\gamma$ Vs K^+K^- phase space. The estimated number of signal events have been added to the 2D mass plot below, with the exception of the $\phi\eta$ intersection region which will be discussed in more detail in the Conclusion section.

2.4 Additional Statistics Study

In addition to the analysis mentioned above, an additional study has been included which simply samples the phase space and records the number of events within that sample. To do this, the same cut ranges as before were used. The only difference is that only the 3x3 grid surrounding the $\phi\eta$ intersection region. Each region is a box cut which is exactly $4\sigma_\phi$ x $4\sigma_\eta$ in area. Each area is given an index to denote the specific region of phase space that is being sampled and an illustration is provided below.

Using the diagram as a reference, it is easy to see that the average number of background events within this phase space can be calculated using the
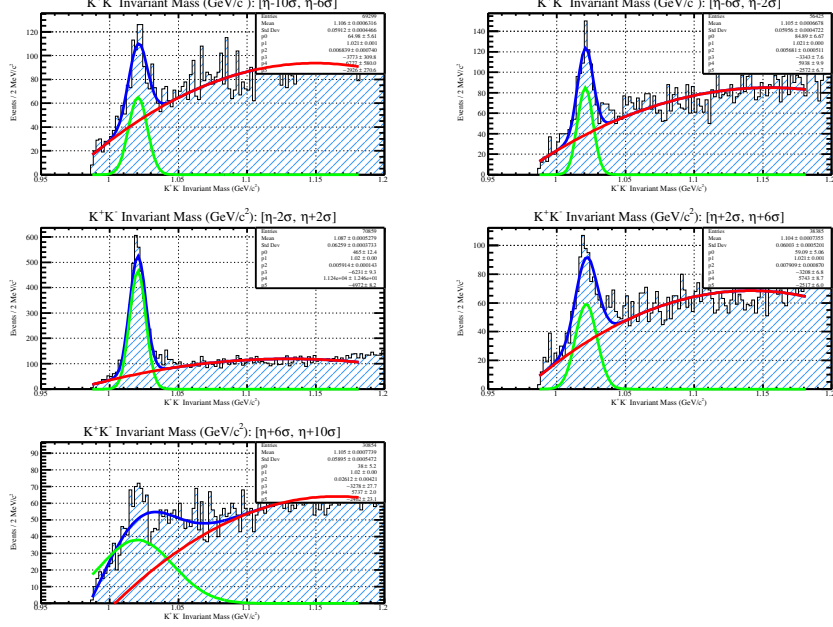
Figure 14: A collection of different K^+K^- Invariant Mass projections as a function of $\gamma_1\gamma_2$ Invariant Mass cut range. Each sub figure includes a red line which is a second degree polynomial used to estimate the shape of the background, a green line which is a Gaussian used to estimate the ϕ signal peak, and a blue line which the sum total of the polynomial fit and Gaussian fit. Lastly, each sub figure also includes the $\gamma_1\gamma_2$ Invariant Mass cut range used to produce the projected figure. This information is in the title of the histogram, inside the brackets.

formula $N_{BG} = (A_1 + A_3 + A_7 + A_9)/4$. Additionally, the average number of ϕ and η events plus background can be calculated using $N_{BG} + N_\phi = (A_4 + A_6)/2$ and $N_{BG} + N_\eta = (A_2 + A_8)/2$, respectively. Lastly, quantification of the number of correlated events in region 5 is possible by using $N_{BG} + N_\phi + N_\eta + N_{correlated} = A_5$. A figure with the number of events contained within each region of phase space is given below.

The first step of this simplistic analysis is to determine what the average number of background events is, which is calculated to be 453. Knowing this, the number of ϕ and η events can now be determined by using the equations $N_{BG} + N_\phi = (A_4 + A_6)/2$ and $N_{BG} + N_\eta = (A_2 + A_8)/2$, and then subtracting the average number of background events. Upon doing
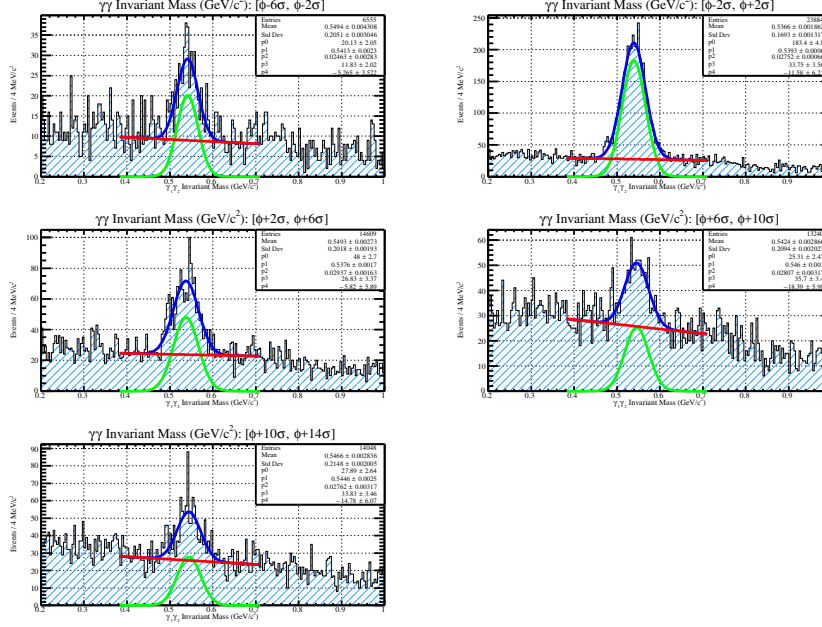
21

Figure 15: A collection of different $\gamma_1\gamma_2$ Invariant Mass projections as a function of K^+K^- Invariant Mass cut range. Each sub figure includes a red line which is a first degree polynomial used to estimate the shape of the background, a green line which is a Gaussian used to estimate the η signal peak, and a blue line which the sum total of the polynomial fit and Gaussian fit. Lastly, each sub figure also includes the K^+K^- Invariant Mass cut range used to produce the projected figure. This information is in the title of the histogram, inside the brackets.

this, it was fount that N_ϕ is 423 and N_η is 433. To complete this analysis, the number of correlated events can now be estimated by using the equation $N_{BG} + N_\phi + N_\eta + N_{correlated} = A_5$, and subtracting N_{BG}, N_ϕ, and N_η. The total number of correlated events is 2446. This calculations shows once again that there is an overflow of events within the $\phi\eta$ intersection region that cannot be explained by the presence of background or the addition of events from the ϕ and η bands.
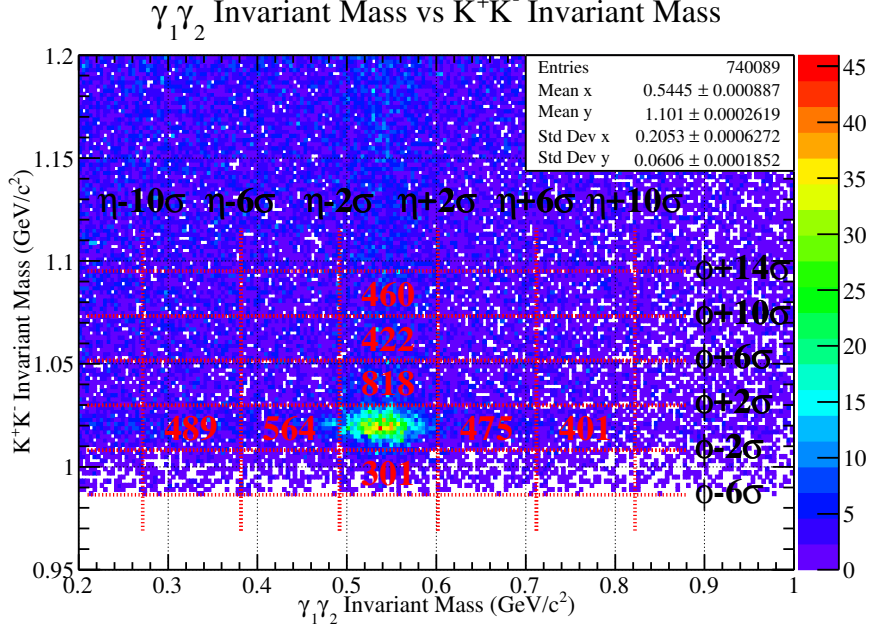
Figure 16: The above figure provides the number of events for each projection range studied. These numbers were calculated by means of integrating the Gaussian fit for either the ϕ or η between $\pm 2\sigma$. The vertical column of numbers represents the number of η events for a given K^+K^- Invariant Mass, and the horizontal row of numbers represents the number of ϕ events for a given $\gamma_1\gamma_2$ Invariant Mass. The number of events observed in the intersection region was not included in the figure due to the amount of space available. There numbers can be found in the Conclusion section.

2.5 Conclusion of K^+K^- Vs $\gamma_1\gamma_2$ Invariant Mass Plot Study

Given that the number of estimated signal events has been calculated for the ϕ and η bands which neighbor the $\phi\eta$ intersection region, the expected number of events will be in the $\phi\eta$ intersection region using averages can be estimated. Taking the numbers from the two dimensional plot above and rounding to the nearest integer, the average number of signal events in the ϕ band is $\overline{\phi_{events}} \sim 482$, and the average number of signal events in the η band is $\overline{\eta_{events}} \sim 500$. Therefore, it is estimated that the number of signal events within the $\phi\eta$ intersection region should be just shy of 1000 events if
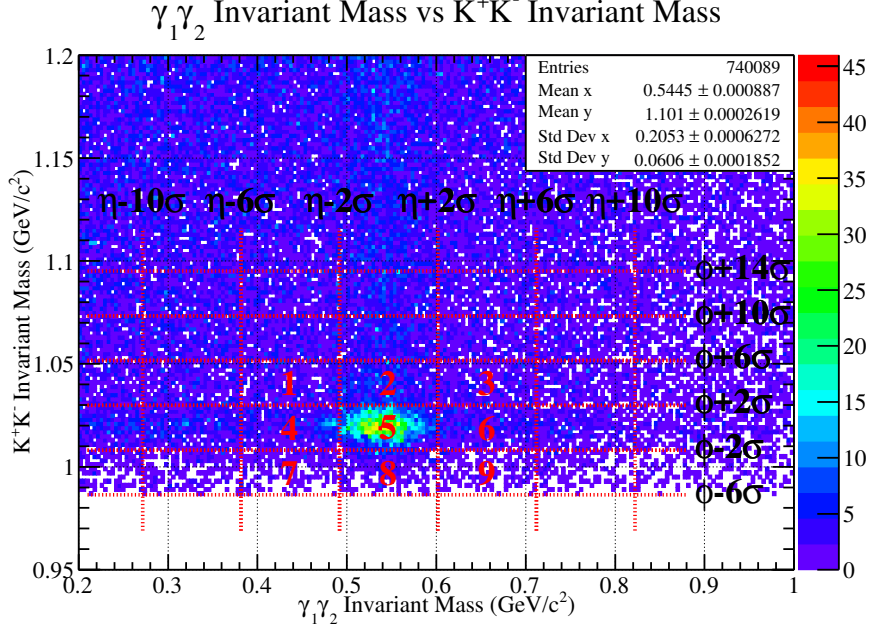
23

Figure 17: An illustration to provide the reader with an idea of how the second statistics study is performed. All of the cut ranges are identical to the first statistics study. The numbers provided in the figure do not represent events, but simply indicate the index associated with a certain area of $\phi\eta$ phase space.

there is no correlation present. After integrating the Gaussian fit for the ϕ and η mesons in the $\phi\eta$ intersection region, it was found that there were 3194 events corresponding to the ϕ fit, and 2993 events corresponding to the η fit. Both of these fits not only yield roughly the same number of events, but they also produce an event estimate which is a factor of three higher than what would have been there from the ϕ and η bands alone. The large increase in event statistics within the $\phi\eta$ intersection region strongly suggests that some type of correlation is present within this area of $K^+K^-\ \gamma\gamma$ phase space. It should be clearly noted that the nature of this correlation is not identified at this time. Moreover, it is unclear from this study as to whether or not the bound stats is mesonic or baryonic in nature. Additional studies on this area of phase space need to be performed in order to establish that this spike in statistics is not coming from the $\gamma p \to N^*\phi$, $N^* \to p\eta$ topology.
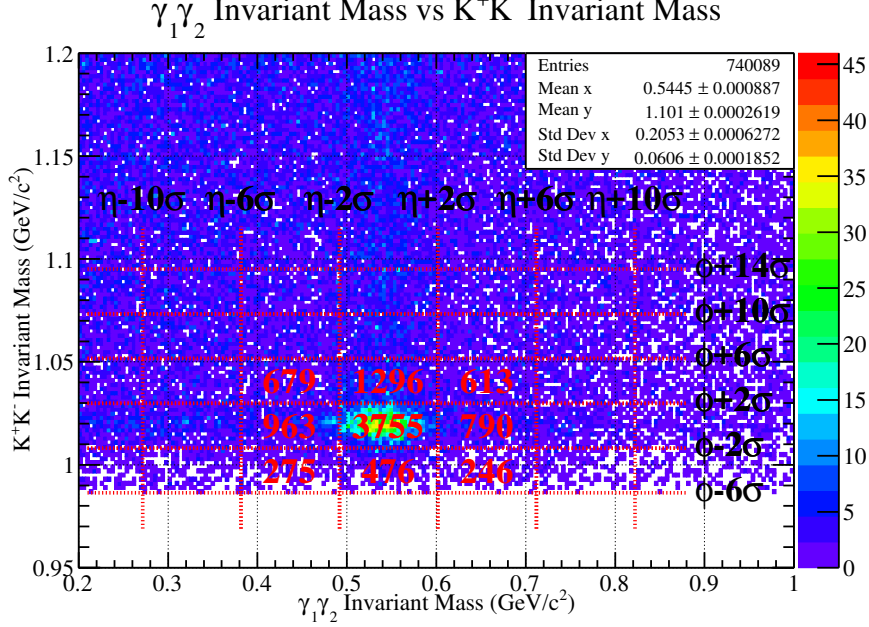
Figure 18: This figure shows the total number of counts in each box. To b be clear, the numbers in each are do not represent the total number of events, but rather the precise amount of statistics contained. Upon inspection, one can see evidence of $\phi\eta$ correlation, which is explained in the Conclusion section.

3 Monte Carlo

3.1 Monte Carlo Features of $\gamma p \to p\phi\eta$

In order to better understand the acceptance of the $\gamma p \to p\phi\eta$ topology in the GlueX spectrometer, a generated Monte Carlo sample was analyzed. More specifically, the exact sample that was produced was $\gamma p \to pX; X \to \phi\eta; \phi \to K^+K^-; \eta \to \gamma\gamma$. This Monte Carlo sample consisted of 170 k generated events for each of the run numbers 030408, 030620, 030802, and 031029. There run numbers were chosen because the first two have beam polarizations in the PARA/PERP directions at low intensity, and the second two have PARA/PERP orientations at high intensity. The total number of generated $\phi\eta$ events is therefore 680 k. The events were generated using a coherent bremsstrahlung beam energy spectrum and a t-slope of 4 $(GeV/c^2)^2$. To be more clear, the thrown beam particles were not polarized in this sample;

only the beam energy spectrum matched that of a polarized beam spectrum (Figure [19]). All final state particle kinematics were generated using the ROOT object TGenPhaseSpace. The generated final state phase space was flat and therefore did not include any spin information from parent or daughter states. The $\gamma, K^+, K^-, \phi, \eta,$ and p particles were generated using the invariant mass values provided in the PDG. The photoproduced X mass was randomly distributed between the lower kinematic limit $m_\phi + m_\eta$ and the upper kinematic limit which is a function of the thrown beam energy.
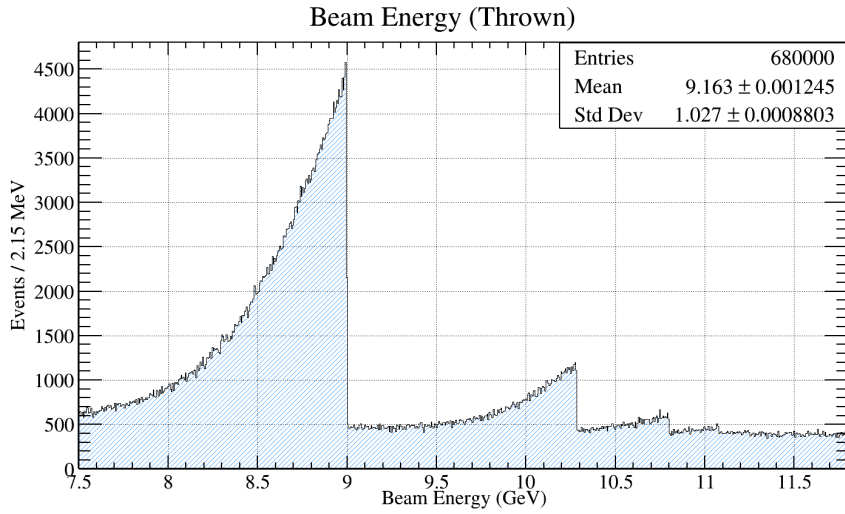

Figure 19: A histogram which includes the thrown beam statistics from the generated Monte Carlo example. In the figure one can easily see the coherent peak which maximizes at 9 GeV. Additionally, one can also see other secondary peaks at higher energy.

An example of what the generated beam energy distribution looks like for this Monte Carlo sample is given in Figure [19]. It should be noted that this particular Monte Carlo sample only generated beam energies between the values of $7.5 - 11.8$ GeV. The reason for the lower energy boundary of the beam energy spectrum is to both cut out potential areas of background due to low energy beam photons and to allow a larger sampling of polarized photons when a beam asymmetry study is performed with actual data. The high energy cut off of 11.8 GeV is simply there to match the high energy cut off of the Spring 2017 run.

Momentum versus theta distributions are also provided in Figures [20], [21], [22], and [23]. These figures are not accepted Monte Carlo, they are only the generates four vectors of the final state particles before running hdgeant, mcsmear, or `hd_root`. Still, the figures provide some insight into the expected
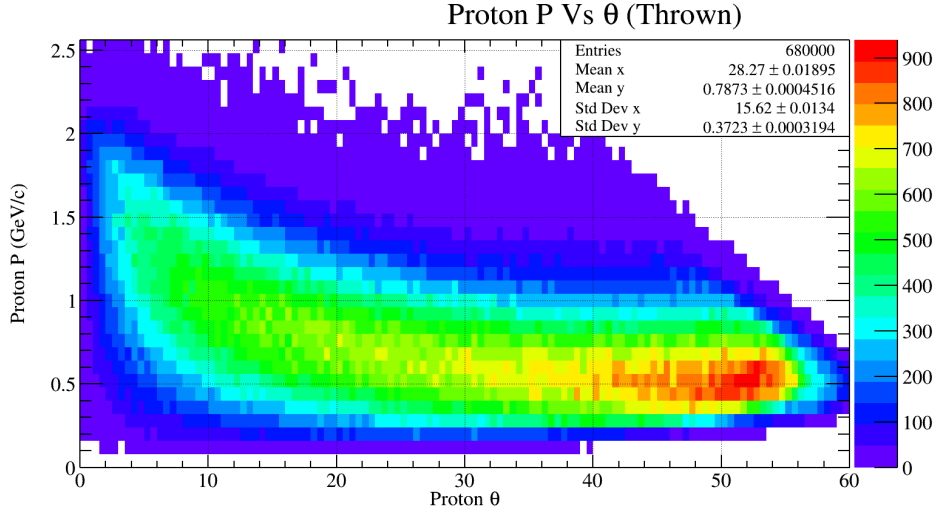
Figure 20: A two dimensional histogram which includes the thrown kinematic information of the recoil proton. In the histogram, the horizontal axis represents the generated θ angle in the lab frame, and the vertical axis represents the generated momentum magnitude in the lab frame. One interesting feature of this Monte Carlo data is that the protons kinematics appear to be constrained between $[0.2 - 2.0]GeV/c$ in momentum, and $[0.0 - 60.0]$ in angle.

kinematic distributions of the final state particles. For example, Figure [20] displays the momentum versus theta distribution for the recoil proton. This figure shows that we should expect the proton to have a very low momentum and high recoil angle relative to the beam direction for this final state.

Additionally. Figures [21][22] show the same plot but for K^+ and K^-, respectively. In these figures, it is clear that Kaons will preferentially travel towards the TOF/FCAL and with a momentum that should include a lot of pion contamination (see Figures [39][46] for more information on pion contamination at high momentum).

Lastly, Figure [23] shows that the final state photons will be mostly forward going and therefore we should expect to see the majority of them interacting with the FCAL rather than the BCAL. It comes as no surprise that the Monte Carlo has generated photons and kaons that favor the forward direction, while the recoil proton has low momentum and a highly transverse direction. This is simply a consequence of the fact that a 'low t' interaction was programmed into the Monte Carlo, resulting in Figure [24].

The last few figures I wish to discuss in this section involve the study of invariant mass spectra. The first of which is the invariant mass of $\phi\eta$

Figure 21: A two dimensional histogram which includes the thrown kinematic information of the generated K^+. In the histogram, the horizontal axis represents the generated θ angle in the lab frame, and the vertical axis represents the generated momentum magnitude in the lab frame.

Figure 22: A two dimensional histogram which includes the thrown kinematic information of the generated K^-. In the histogram, the horizontal axis represents the generated θ angle in the lab frame, and the vertical axis represents the generated momentum magnitude in the lab frame.

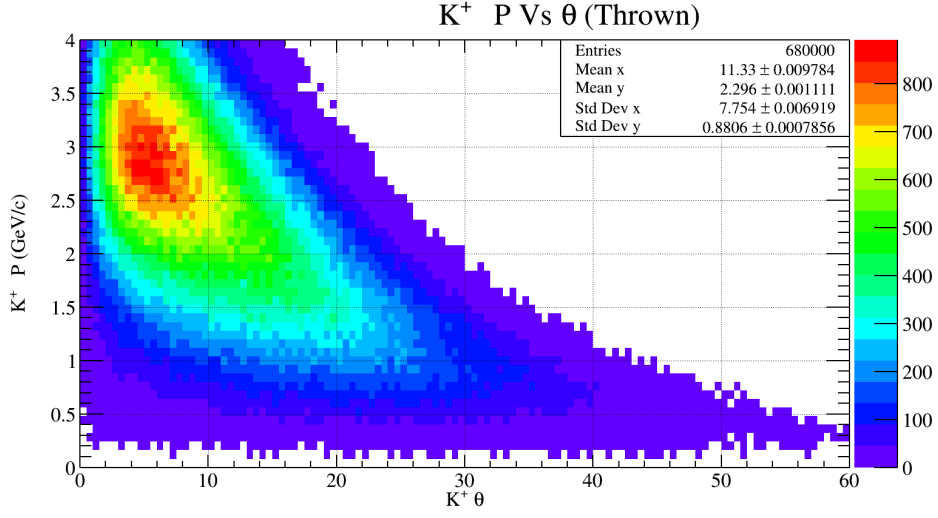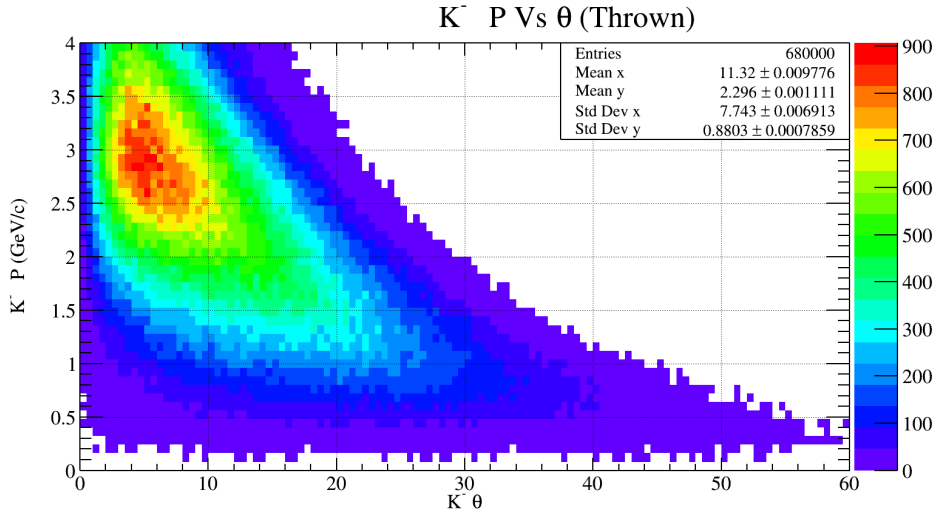(Figure [25]) which shows a flat distribution between the values of 1.5 to
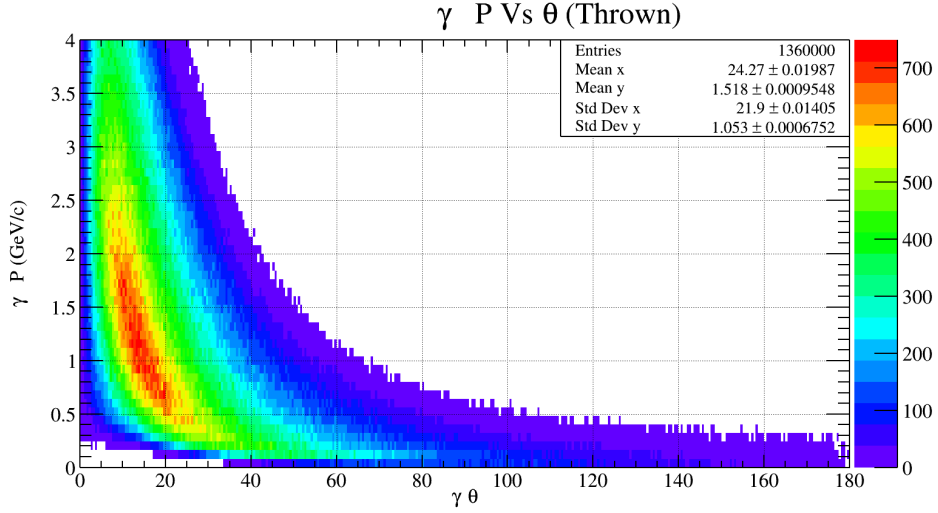
Figure 23: A two dimensional histogram which includes the thrown kinematic information of the generated photons. In the histogram, the horizontal axis represents the generated θ angle in the lab frame, and the vertical axis represents the generated momentum magnitude in the lab frame.
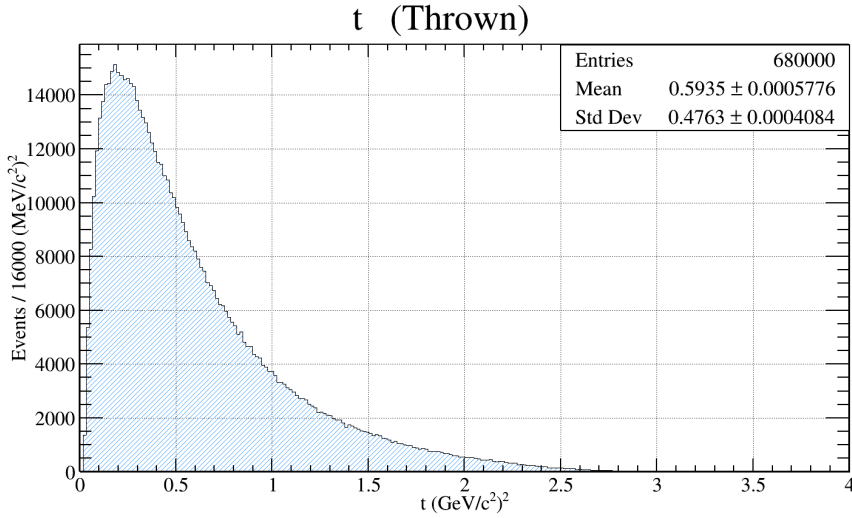
Figure 24: A histogram which includes the generated spectrum for the Mandelstam variable, t. The most important feature in this histogram is the fact that the majority of generated events come from low momentum transfer.

3 GeV/c^2; then the distribution drops off drastically until 3.3 GeV/c^2; and then less drastically from 3.3 to 4 GeV/c^2. These features may seem incor-

rect at first glance since the generated Monte Carlo mass is supposed to be flat. However, upon further inspection, it is clear that these features manifest themselves within the Monte Carlo data because of the shape of the beam spectra. The best way to see this behaviour is by considering Figure [26]. This figure shows the generated mandelstam variable t on the vertical axis, and the generated $\phi\eta$ mass on the horizontal axis. Since t is the momentum transfer, it is directly correlated with the beam photon and therefore will exhibit some coherent bremsstrahlung structure. This structure can be seen in Figure [26] where there is clear evidence of the beam energy spectra influencing the behavior of the $\phi\eta$ mass. We know from Figure [19] that the most dominant statistics will come from the coherent edge at 9 GeV and should drop off drastically beyond that point. This feature of the data is clearly seen in Figure [26] and is therefore the reason for the odd behavior seen in Figure [25].
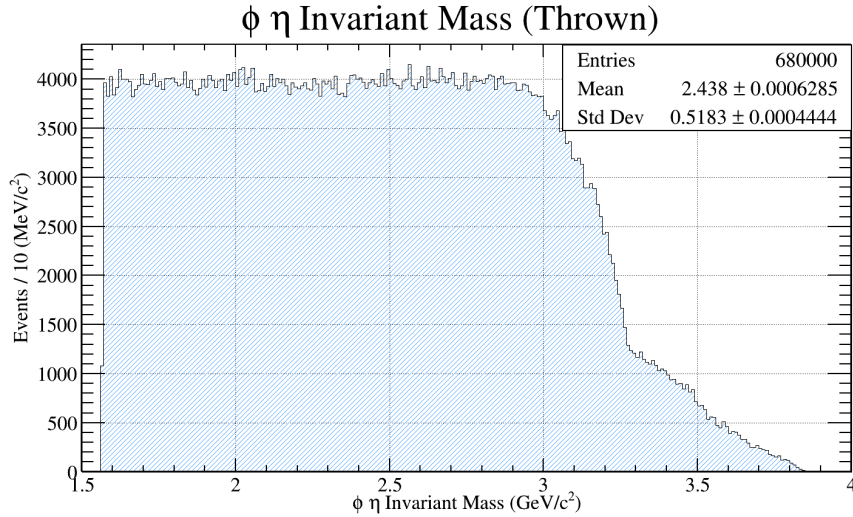
Figure 25: A histogram which includes the generated $\phi\eta$ invariant mass. In the figure one can easily see that the invariant mass of the $\phi\eta$ remains flat until it reaches $\sim 3.0 GeV/c^2$. From that point, the invariant mass falls sharply until $\sim 3.3 GeV/c^2$; and then continues to fall at a slower rate. This feature of the invariant mass is directly related to the fact that a coherent bremsstrahlung beam energy spectrum was used. The drastic drop off in statistics in the mass range of $3.0 - 3.3 GeV/c^2$ is caused by the primary coherent peak at $9.0 GeV$. To visualize this more clearly, see Figure [26].

30
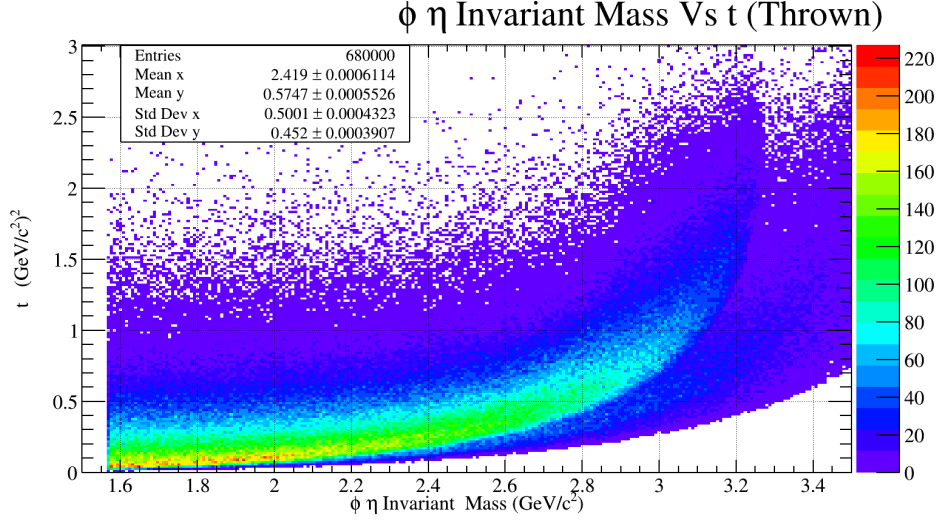
Figure 26: A two dimensional histogram which includes the generated $\phi\eta$ invariant mass on the horizontal axis and the Mandelstam t variable on the vertical axis. In the figure one can easily see the effect that the coherent peak has on the shape of the phase space. The effect can be seen in even greater detail in Figure [25].

3.2 A Monte Carlo Study to Determine ΔT Cuts

The timing cut values listed in Table [1] were determined by performing a full reconstruction of the Monte Carlo data discussed in the previous section. The procedure for reconstructing the Monte Carlo data is well known. First the four vectors of the $\gamma p \to pX; X \to \phi\eta; \phi \to K^+K^-; \eta \to \gamma\gamma$ topology are generated using TGenPhaseSpace. Next, the four vectors are fed into hdgeant where interactions with the detector are considered and all detector hits are interpreted using the geometry. After hdgeant completes, the Monte Carlo is then passed into mcsmear; which is responsible for taking the 'perfect' data from hdgeant and changing it to match the resolution of GlueX sub detectors. Upon mcsmear completion, the Monte Carlo procedure enters its final stage of reconstruction. This is done by calling the `hd_root` command coupled with a few plugins including `dana_rest`.

3.3 Evidence of Secondary Photons

Before performing this Monte Carlo study, it was well known that there was a lot of photon background seen in the data. After studying the data for quite some time, it was found that a two photon cut would destroy most
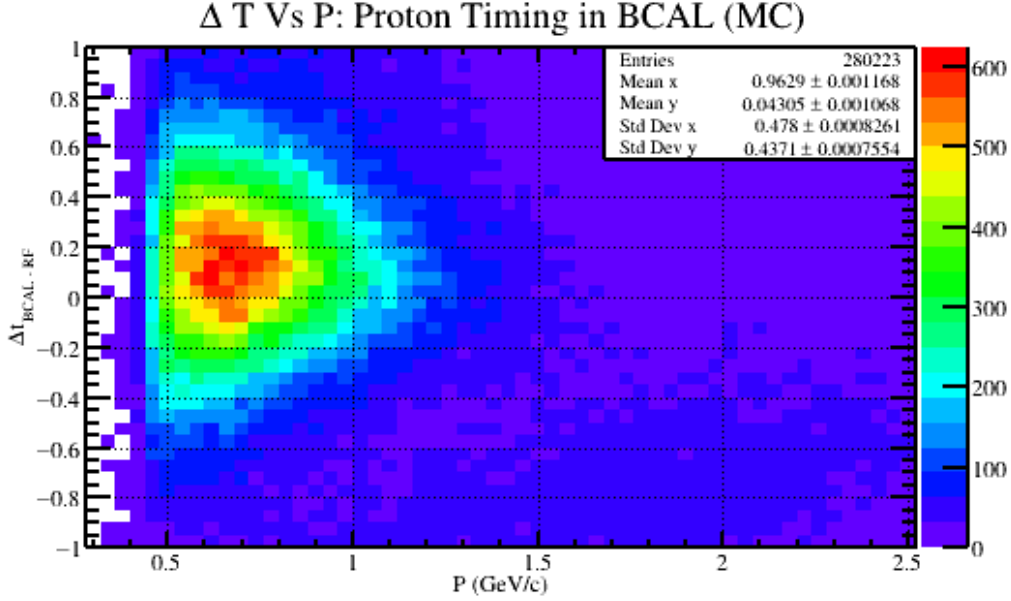
Figure 27: A timing plot for generated protons after reconstruction. The horizontal axis is the reconstructed momentum of the proton and the vertical axis is the timing difference between the BCAL and RF. The enhancement of statistics in the lower right portion of the plot comes from miss identified kaons that were also included in the Monte Carlo.

of the background associated with photons and would also result in an observed η resonance in a $\gamma\gamma$ invariant mass plot. At the time, it was unknown why the cut appeared to throw out a lot of photon background while simultaneously appearing to enhance signal. After carefully studying accepted Monte Carlo, background generated Monte Carlo (`bggen`), and data, it was found that much of this background is attributed to secondary photons. A secondary photon should be thought of as a photon that did not originate from any photoproduction reaction, nor from any expected decay of parent states. Therefore, a secondary photon can be thought of as a photon that arose from an interaction within the GlueX spectrometer from a final state particle. An example of a secondary photon that would be present in $\gamma p \rightarrow p\phi\eta$ data can be explained by means of high momentum and forward going kaons (Figures [21][22]). Since it is very likely that most of the kaons in this channel will interact with either the Time of Flight detector or the Forward Calorimeter, it is expected that these particle will deposit a lot of energy in this region of the spectrometer. These high momentum particles will cause a signal in one or both of these detectors and will also cause a
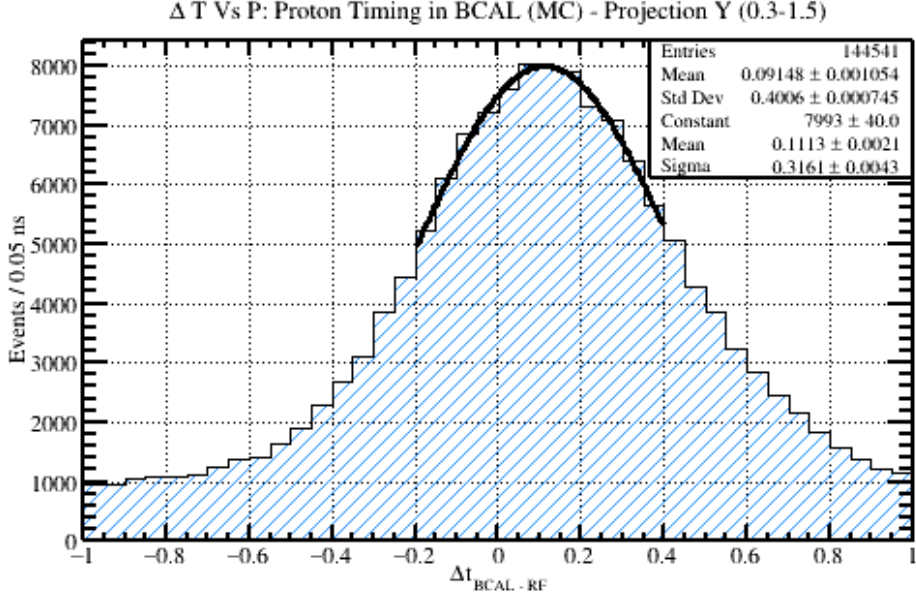
32

Figure 28: A projection of the statistics from Figure [27] onto the vertical (timing) axis between the momentum range of 0.3-1.5 GeV/C. This projection range was chosen so that the distortion from the lower kaon band was minimized. A Gaussian fit was performed and is included in the figure where the mean and width of the distribution are given in the legend.

'splash' effect near the signal region. This splash effect can cause some of the blocks in the Forward Calorimeter to absorb the extra energy and therefore become reconstructed photons in the data. The additional reconstructed photons will therefore cause the number of photons reconstructed in an event to be fictitiously higher than what was actually present within the detector. To first order, this perhaps explains why doing a two photon cut on data will both greatly reduce background and enhance a signal. However, many important questions will still remain about this cut. How much signal do we lose by simply performing a two photon cut? Furthermore, is there a better way to cut out the background and preserve as many signal events as possible? This subsection will show that this effect does in fact manifest itself in both Monte Carlo and data; and will perform an analysis on Monte Carlo and data to show the best way of reducing secondary photons.

The first evidence that suggests the existence of secondary photons in $\gamma p \rightarrow p\phi\eta; \phi \rightarrow K^+K^-; \eta \rightarrow \gamma\gamma$ accepted Monte Carlo can be seen by simply plotting the invariant mass of a reconstructed $\gamma\gamma$ pair (Figure [51]). The data which went into this plot was created by throwing $\gamma p \rightarrow p\phi\eta; \phi \rightarrow$
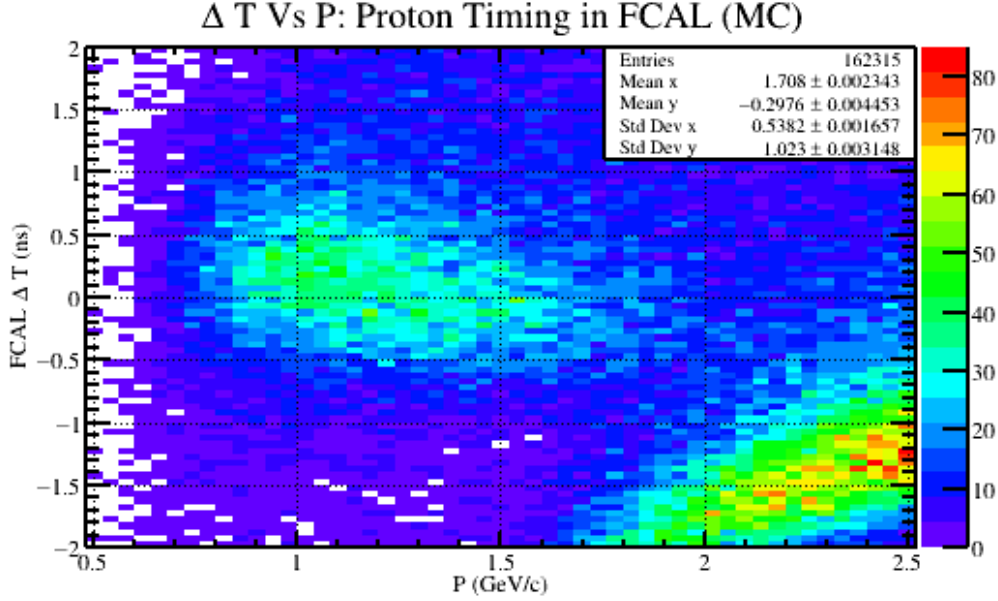
Figure 29: A timing plot for generated protons after reconstruction. The horizontal axis is the reconstructed momentum of the proton and the vertical axis is the timing difference between the FCAL and RF. The enhancement of statistics in the lower right portion of the plot comes from miss identified kaons that were also included in the Monte Carlo.

K^+K^-; $\eta \to \gamma\gamma$ into the GlueX detector and then simulating its behavior with `hdgeant` and `mcsmear`. The invariant mass spectrum in Figure [51] shows a clear peak from the generated η meson on top of a background that spans to low mass. If this sample initially only threw two photons exactly equal to the η meson invariant mass, then why are there so many low mass photon combinations that appear to be in the shape of background? To answer this question, we can separate our reconstructed Monte Carlo particles into two categories: particles that were generated and particles that were not generated. In doing so, we can see where this background comes from and also how to possibly reduce it.

We will first describe the background seen in Figure [51] by displaying P Vs θ and ϕ Vs θ plots for the thrown photons and the secondary photons in Figure [52]. The most important feature to take away from these plots is the tendency for secondary photons to be at a shallow angle relative to the beam direction (below 12°) while also having a low three momentum magnitude (below 500 MeV/c). Simply knowing the distribution of these photons gives us some insight into where they came from. Since neutral photons can only
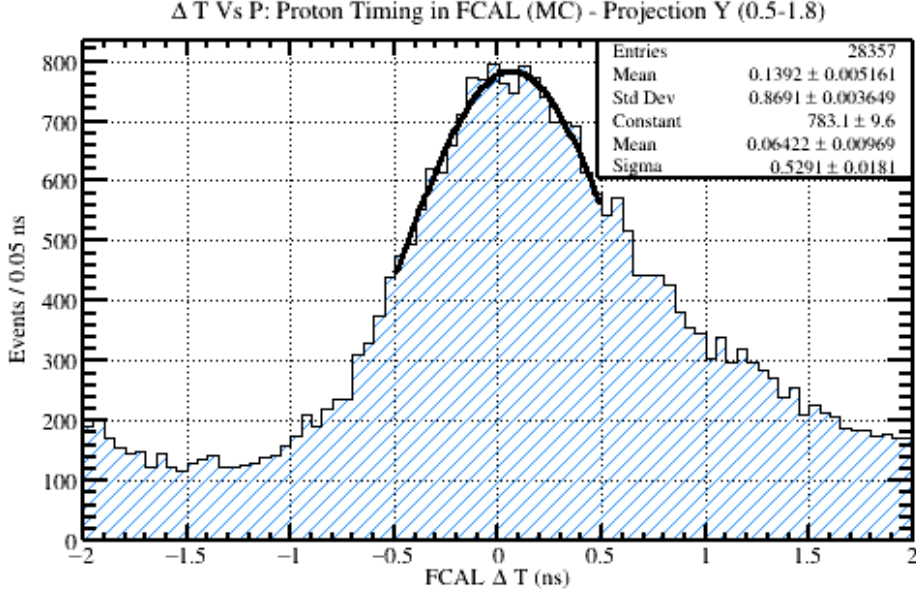
34

Figure 30: A projection of the statistics from Figure [29] onto the vertical (timing) axis between the momentum range of 0.5-1.8 GeV/C. This projection range was chosen so that the distortion from the lower kaon band was minimized. A Gaussian fit was performed and is included in the figure where the mean and width of the distribution are given in the legend.

be detected by either the Forward Calorimeter or the Barrel Calorimeter and most of these photons appear in the forward direction, it is clear that FCAL showers are causing these photons to appear.

The reconstructed invariant mass for a given $\gamma\gamma$ combination within an event as a function of the number of photons reconstructed within an event can also be shown. By using our Monte Carlo samples, we can also separate these plots into thrown and secondary photons, identical to what we did in Figure [52]. The reconstructed invariant mass of two photons versus the number of reconstructed photons in an event is given in Figure [53]. There are two important observations that should be taken away from the two sub figures. In Figure 53a a clear η resonance can be seen which spans a large number of reconstructed photons per event. What this sub figure tells us right away is that performing a two photon cut on the data is not good for signal events. In fact, after fitting a Gaussian function to the η peaks between 3 and 10 reconstructed photons, it was found that ∼8,000 combinations would be lost out of a total of ∼30,000; resulting in a 26 percent loss of events. The second important feature seen in Figure 53b is the fact that most of the
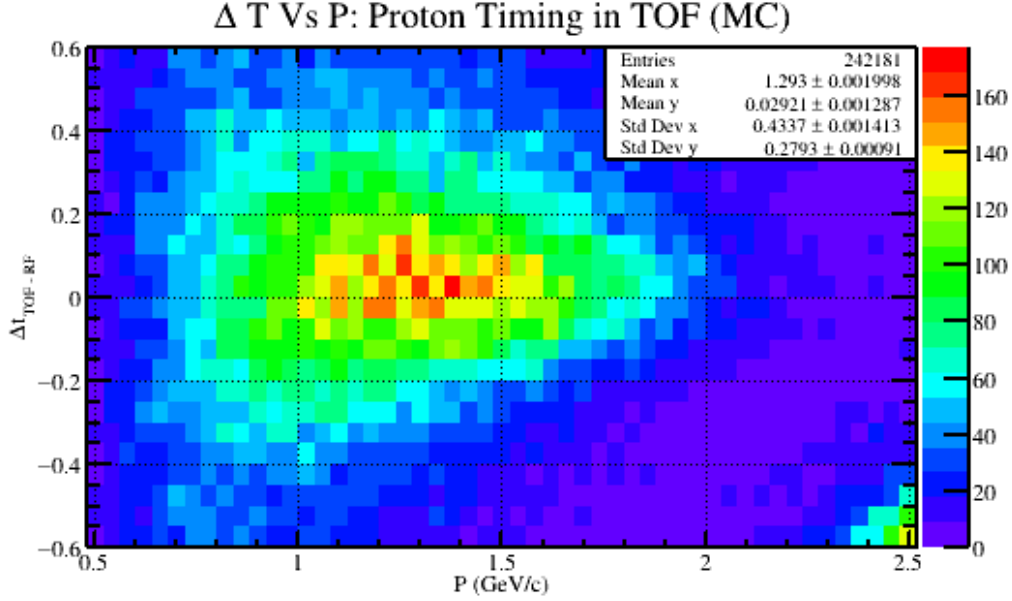
Figure 31: A timing plot for generated protons after reconstruction. The horizontal axis is the reconstructed momentum of the proton and the vertical axis is the timing difference between the TOF and RF. The enhancement of statistics in the lower right portion of the plot comes from miss identified kaons that were also included in the Monte Carlo.

secondary photons exist in events which reconstruct more than two photons per event. Therefore, it is imperative to cut secondary photons while also preserving the event photons that exist in events which yield a large number of reconstructed photons.

There are a number of ways to cut the secondary photons seen in accepted Monte Carlo. The first and most obvious way would be to cut photons that are both below 12° θ and lower than 500 MeV/c in three momentum magnitude. However, since this analysis will eventually include a cut on Kinematic Fit confidence level, the effect of this cut on secondary photons will be studied first. This portion of the study will now include three sets of data: accepted Monte Carlo, background generated Monte Carlo bggen, and data. The fist plot that will be shown is the Kinematic Fit confidence level versus the reconstructed $\gamma_1 \gamma_2$ invariant mass for all three data sets (Figure [54]). In each plot one can easily see an η peak at higher confidence level along side background which is typically at much lower confidence level. Using the accepted Monte Carlo from Figure [54a] it was determined that a preliminary Kinematic Fit confidence level cut would be placed at the value
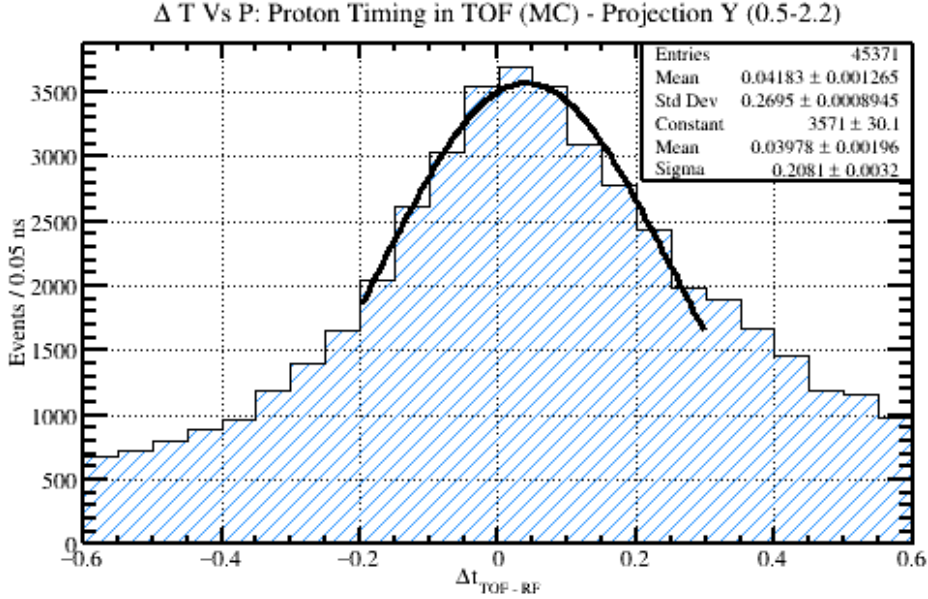
36

Figure 32: A projection of the statistics from Figure [31] onto the vertical (timing) axis between the momentum range of 0.5-1.8 GeV/C. This projection range was chosen so that the distortion from the lower kaon band was minimized. A gaussian fit was performed and is included in the figure where the mean and width of the distribution are given in the legend.

$1x10^{-6}$.

After performing a confidence level cut of $1x10^{-6}$ it is clear that much of the secondary photons are destroyed. One way of seeing the effect of this cut is by looking at the number of reconstructed photons in an event versus the $\gamma_1\gamma_2$ invariant mass distributions (Figure [55]). Comparing Figure [55a] with Figure [53a], one can easily see that the Kinematic Fit confidence level cut moved many of the η's from high photon reconstruction number per event to low photon reconstruction number per event. This migration of events is due to the fact that the Kinematic Fitter is cutting many secondary photons out of events and therefore decreasing the number of photons reconstructed per event. Furthermore, comparing Figure [55b] with Figure [53b], one can simply look at the density of events within the two dimensional histogram to realize that an overwhelming amount of secondaries has been cut, roughly 94 percent.

Seeing that there is still a non negligible amount of secondary photons left in accepted Monte Carlo and `bggen`, the next cut that will be applied to all of the data is a P Vs θ cut, where $P < 500 MeV/c$ and $\theta < 12$ °. After
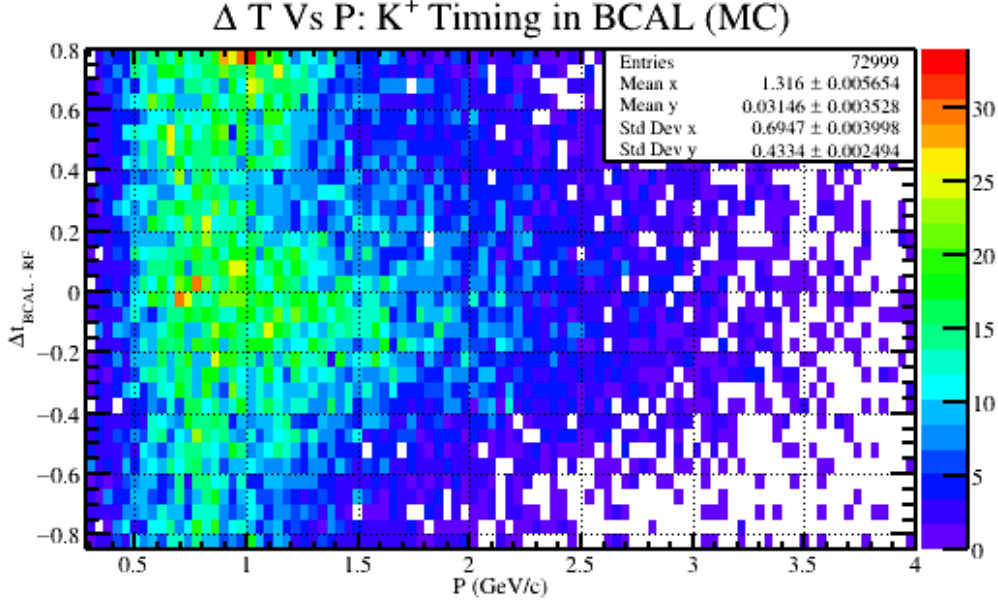
37

Figure 33: A timing plot for generated K^+ after reconstruction. The horizontal axis is the reconstructed momentum of the K^+ and the vertical axis is the timing difference between the BCAL and RF. It should be noted that the statistics in this sampling are smaller than other plots. This is due to the fact that the kinematics of the generated channel prefer to have the kaons moving in the forwards direction; and therefore provide few timing hits in the BCAL. Additionally, the extra statistics present in the upper left portion of the graph are due to protons included in this Monte Carlo sample.

enforcing these cuts on all photons, the distribution of number of photons reconstructed in an event versus $\gamma_1\gamma_2$ Invariant Mass is shown once again in Figure [56]. It is easy to see that most, if not all of the η signal has migrated to the two photon bin and simultaneously much of the secondary background has been reduced in all data sets. Due to this, a two photon cut is now necessary to do in order to reduce some of the left over background at higher number of reconstructed photons per event.

In this section it was shown that it is necessary to perform a Kinematic Fit confidence level cut; followed by a P Vs θ cut of $P < 500 MeV/c$ and $\theta < 12$ °; and finally a two photon cut. After completing this sequence of cuts, it was found that 94 percent of background data was cut, while preserving 93 percent of signal data.
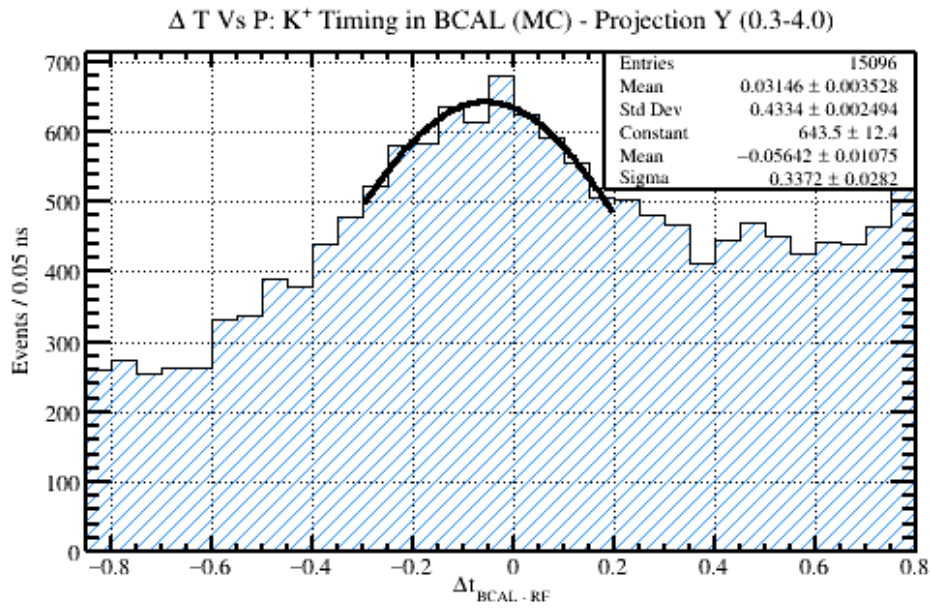
Figure 34: A projection of the statistics from Figure [33] onto the vertical (timing) axis between the momentum range of 0.3-4.0 GeV/C. A Gaussian fit was performed and is included in the figure where the mean and width of the distribution are given in the legend. The distortion of statistics towards the higher timing differences is due to protons included in this Monte Carlo study.

Figure 35: A timing plot for generated K^+ after reconstruction. The horizontal axis is the reconstructed momentum of the K^+ and the vertical axis is the timing difference between the FCAL and RF. The curved band that appears below the K^+ band around 1.5 GeV/c and lower comes from π^+. Although pions were not explicitly generated, the computer program hdgeant (derived from geant) allows for some fraction of kaons to decay weakly while in flight; resulting in an observed pions.

ΔT Vs P: K$^+$ Timing in FCAL (MC) - Projection Y (2.0-4.0)

| Entries	22586
Mean	-0.006254 ± 0.005521
Std Dev	0.8297 ± 0.003904
Constant	759.3 ± 9.4
Mean	-0.2517 ± 0.0053
Sigma	0.4114 ± 0.0076

Figure 36: A projection of the statistics from Figure [35] onto the vertical (timing) axis between the momentum range of 2.0-4.0 GeV/C. This projection range was chosen so that the distortion from the lower pion band and upper proton band was minimized. A Gaussian fit was performed and is included in the figure where the mean and width of the distribution are given in the legend.
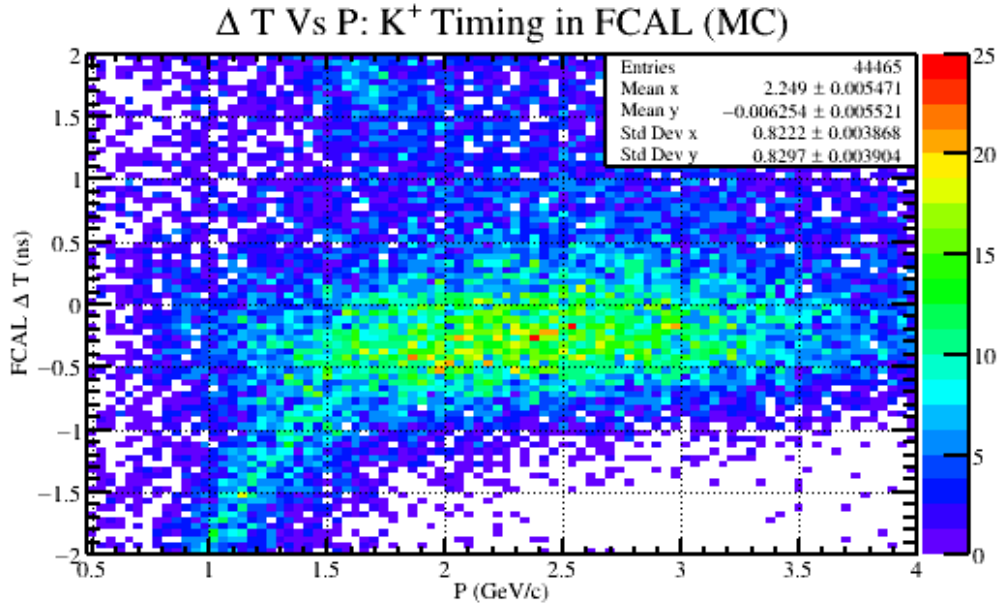
41
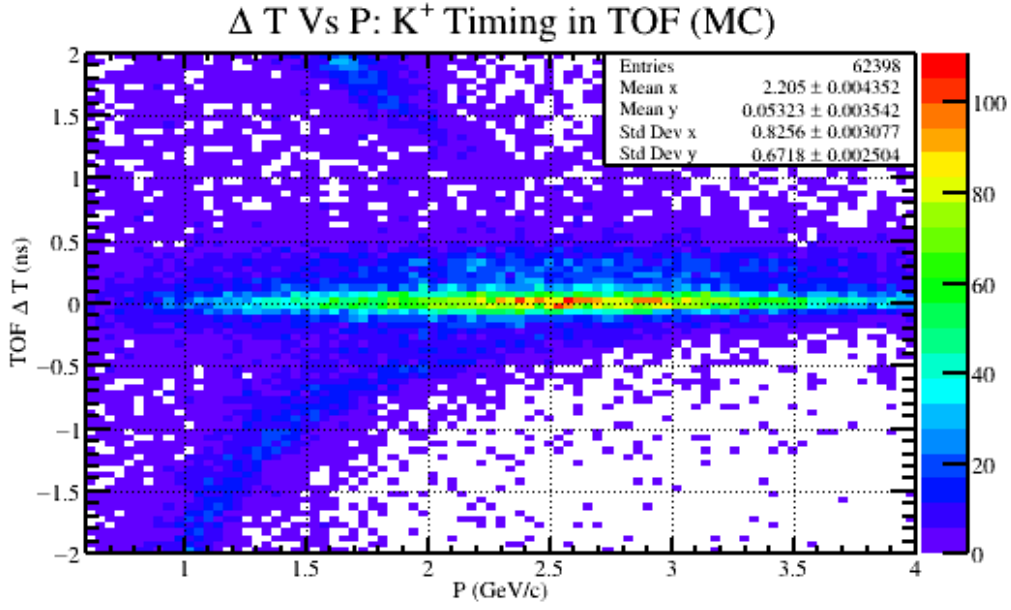
Figure 37: A timing plot for generated K^+ after reconstruction. The horizontal axis is the reconstructed momentum of the K^+ and the vertical axis is the timing difference between the TOF and RF. The curved band that appears below the K^+ band around 2.5 GeV/c and lower comes from π^+; and the band near the top of the plot comes from protons. Although pions were not explicitly generated, the computer program hdgeant (derived from geant) allows for some fraction of kaons to decay weakly while in flight; resulting in an observed pions.
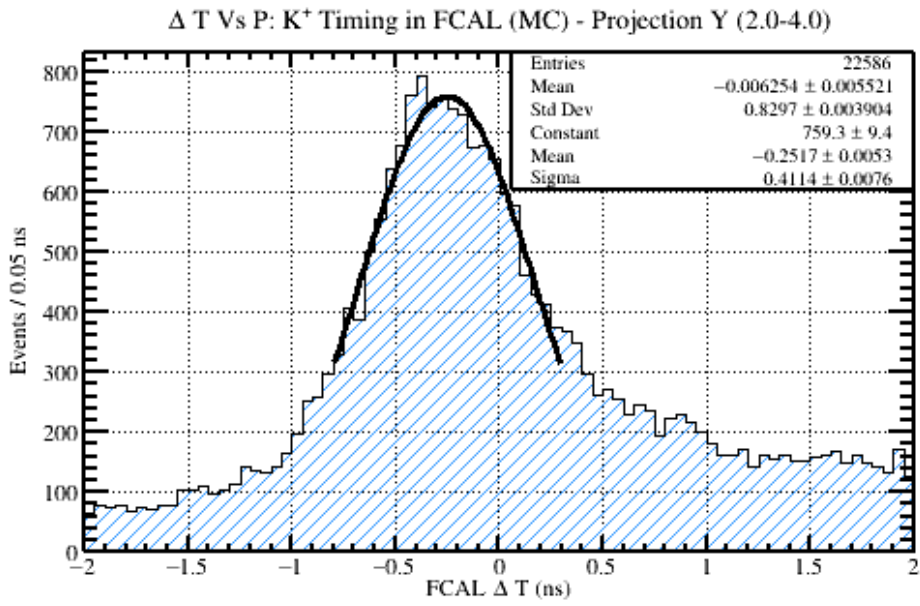
ΔT Vs P: K⁺ Timing in TOF (MC) - Projection Y (1.9-2.0)

Entries	1909
Mean	0.2969 ± 0.01747
Std Dev	0.7634 ± 0.01235
Constant	41.22 ± 3.86
Mean	-0.5558 ± 0.0113
Sigma	0.1196 ± 0.0131
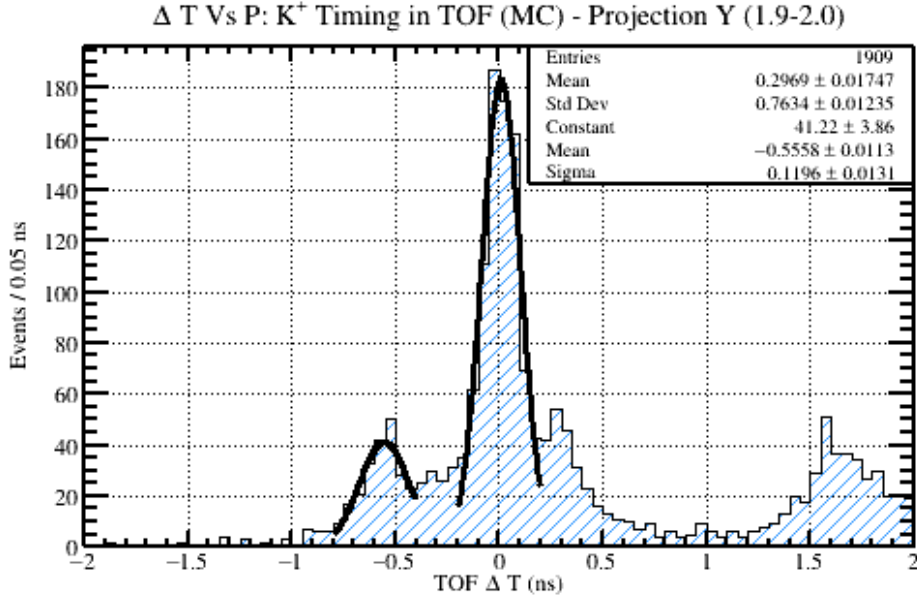
Figure 38: A projection of the statistics from Figure [37] onto the vertical (timing) axis between the momentum range of 1.9-2.0 GeV/C. This projection range is one out of many that were studied from Figure [37]. The purpose of this study is to determine the amount of pion contamination in the kaon band as a function of momentum. The results of this study are provided in Figure [39]. Lastly, two Gaussian fits were performed on this data. The mean and width of these Gaussian fits are recorded in Figure [39] for each momentum range.

Figure 39: The image above is the result of the timing study performed on Figure [37]. Using that figure, a number of projection histograms were fit using different momentum ranges. An example of one of these fits is given in Figure [38]. The data points close to 0 ΔT correspond to t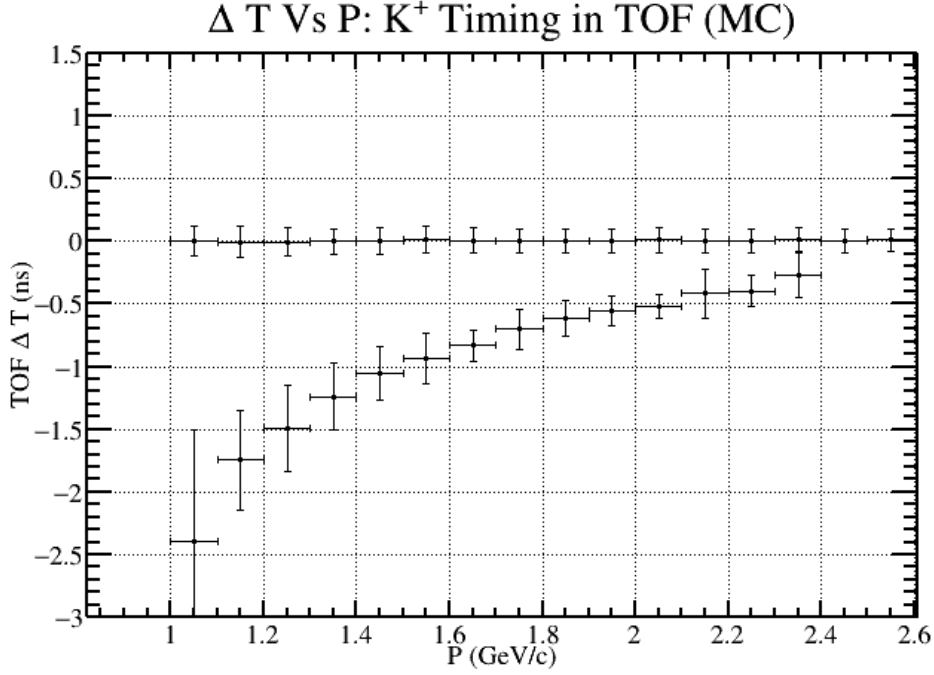he Gaussian fits performed on the kaon signal, and the data points that approach that band from the bottom correspond to the Gaussian fits performed on the pion signal. The horizontal position of each point is in the middle of the projection range, and the vertical position of each point was assigned based on the mean value of the Gaussian fit for each particle. The horizontal error bars are the size of the projection range, which is always 0.1 GeV/c. The vertical error bars are determined by the width of the Gaussian fits. The average of the widths of the kaon peaks is $0.1 ns$ which is the value used to determine the timing cut in Table 1.

44

Figure 40: A timing plot for generated K^- after reconstruction. The horizontal axis is the reconstructed momentum of the K^- and the vertical axis is the timing difference between the BCAL and RF. It should be noted that the statistics in this sampling are smaller than other plots. This is due to the fact that the kinematics of the generated channel prefer to have the kaons moving in the forwards direction; and therefore provide few timing hits in the BCAL. Additionally, the extra statistics present in the lower left portion of the graph are due to pions. Although pions were not explicitly generated, the computer program hdgeant (derived from geant) allows for some fraction of kaons to decay weakly while in flight; resulting in an observed pions.

Figure 41: A projection of the statistics from Figure [40] onto the vertical (timing) axis between the momentum range of 0.3-4.0 GeV/C. A Gaussian fit was performed and is included in the figure where the mean and width of the distribution are given in the legend.
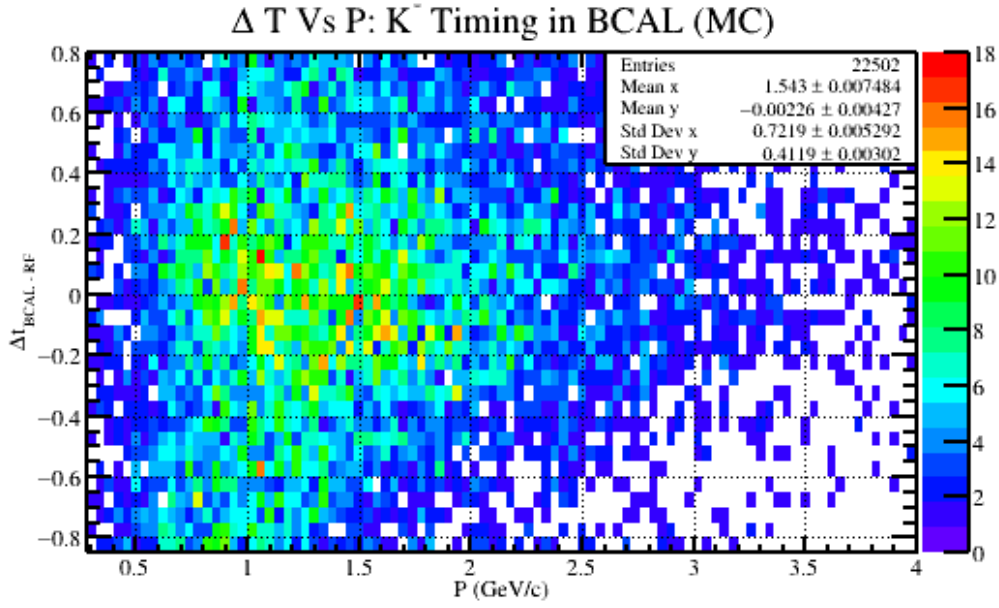
Figure 42: A timing plot for generated K^- after reconstruction. The horizontal axis is the reconstructed momentum of the K^- and the vertical axis is the timing difference between the FCAL and RF. The curved band that appears below the K^- band around 1.5 GeV/c and lower comes from π^-. Although pions were not explicitly generated, the computer program hdgeant (derived from geant) allows for some fraction of kaons to decay weakly while in flight; resulting in an observed pions.
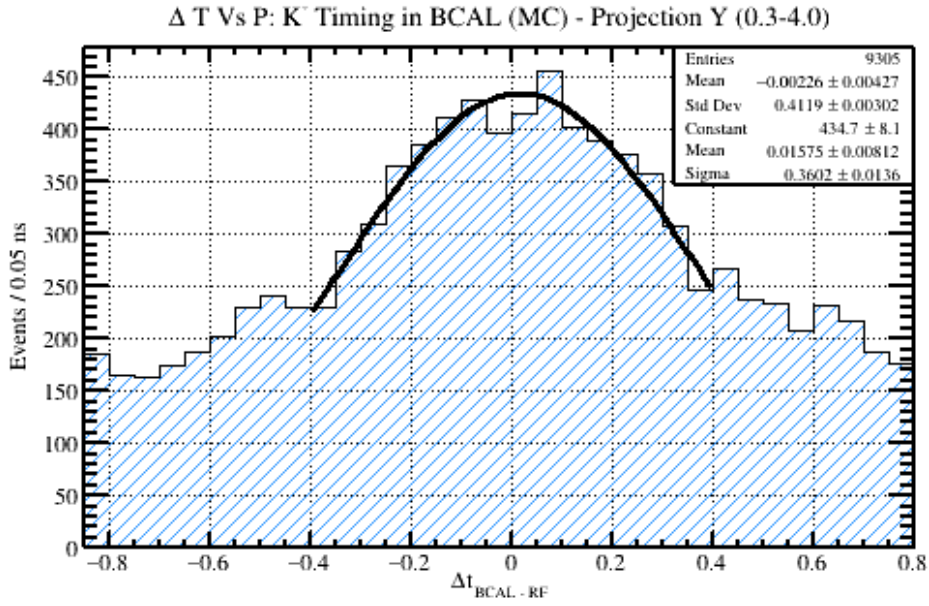
Figure 43: A projection of the statistics from Figure [42] onto the vertical (timing) axis between the momentum range of 2.0-4.0 GeV/C. This projection range was chosen so that the distortion from the lower pion band was minimized. A Gaussian fit was performed and is included in the figure where the mean and width of the distribution are given in the legend.
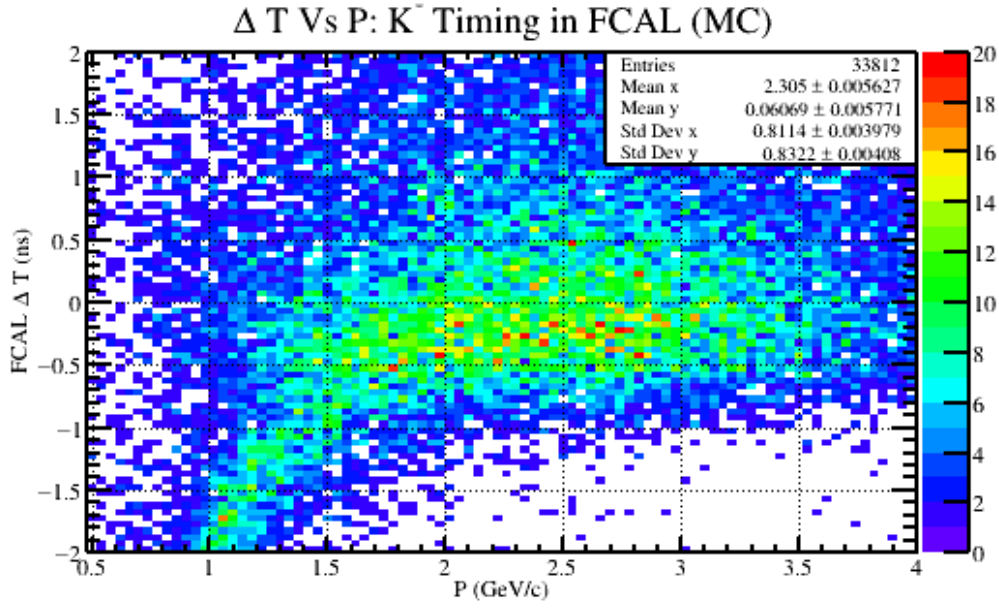
48

Figure 44: A timing plot for generated K^- after reconstruction. The horizontal axis is the reconstructed momentum of the K^- and the vertical axis is the timing difference between the TOF and RF. The curved band that appears below the K^- band around 2.5 GeV/c and lower comes from π^-. Although pions were not explicitly generated, the computer program hdgeant (derived from geant) allows for some fraction of kaons to decay weakly while in flight; resulting in an observed pions.
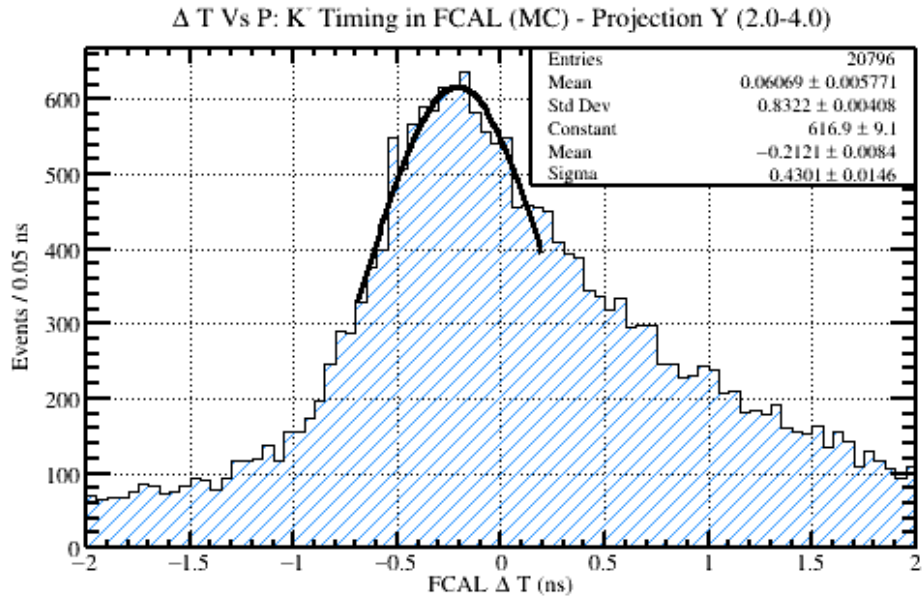
49
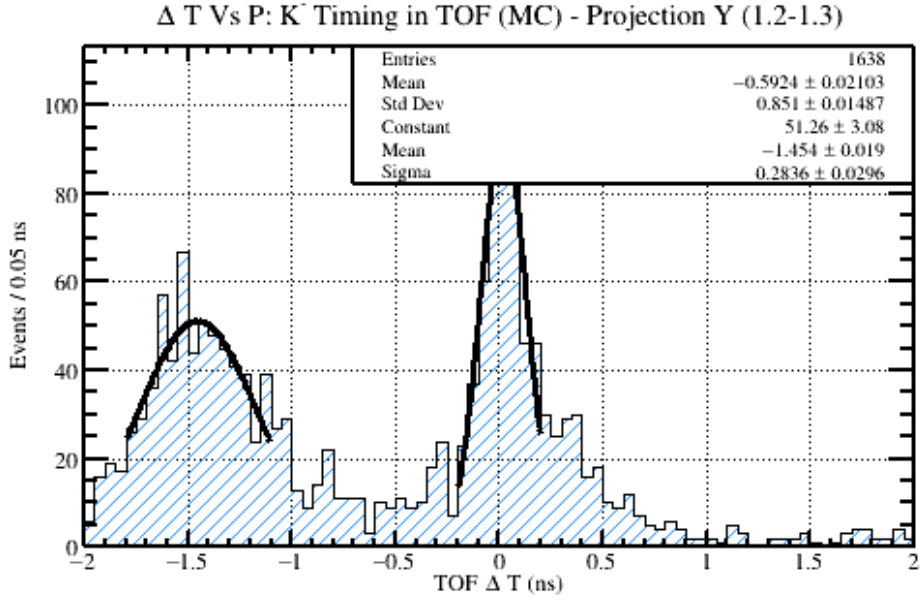
Figure 45: A projection of the statistics from Figure [44] onto the vertical (timing) axis between the momentum range of 1.2-1.3 GeV/C. This projection range is one out of many that were studied from Figure [44]. The purpose of this study is to determine the amount of pion contamination in the kaon band as a function of momentum. The results of this study are provided in Figure [46]. Lastly, two Gaussian fits were performed on this data. The mean and width of these Gaussian fits are recorded in Figure [46] for each momentum range.

Figure 46: The image above is the result of the timing study performed on Figure [44]. Using that figure, a number of projection histograms were fit using different momentum ranges. An example of one of these fits is given in Figure [45]. The data points close to 0 ΔT correspond to the Gaussian fits performed on the kaon signal, and the data points that approach that band from the bottom correspond to the Gaussian fits performed on the pion signal. The horizontal position of each point is in the middle of the projection range, and the vertical position of each point was assigned based on the mean value of the Gaussian fit for each particle. The horizontal error bars are the size of the projection range, which is always 0.1 GeV/c. The vertical error bars are determined by the width of the Gaussian fits. The average of the widths of the kaon peaks is 0.1ns which is the value used to determine the timing cut in Table 1.
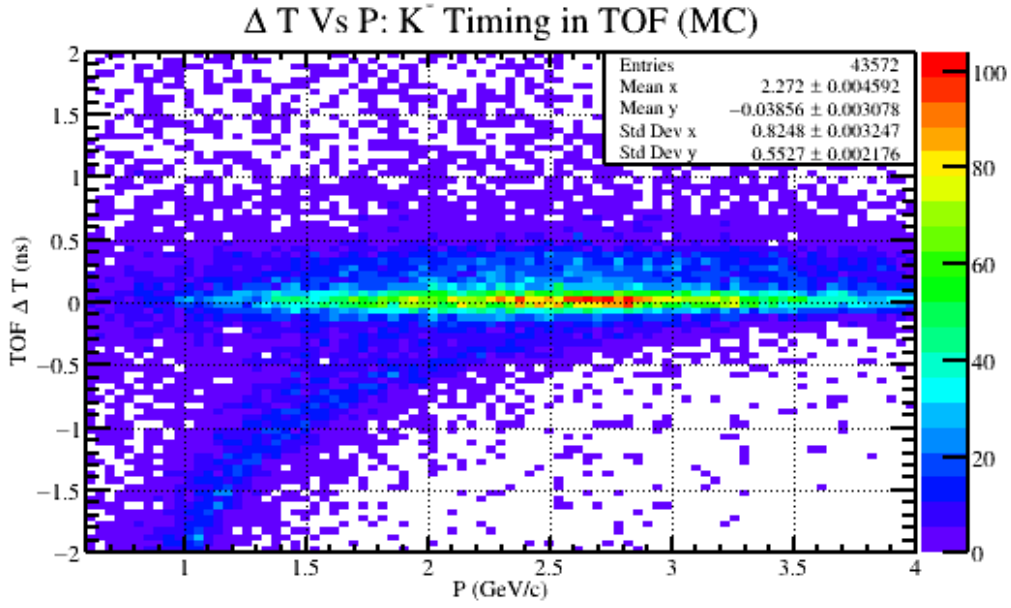
51

Figure 47: A timing plot for generated γ after reconstruction. The horizontal axis is the reconstructed momentum of the γ and the vertical axis is the timing difference between the BCAL and RF.
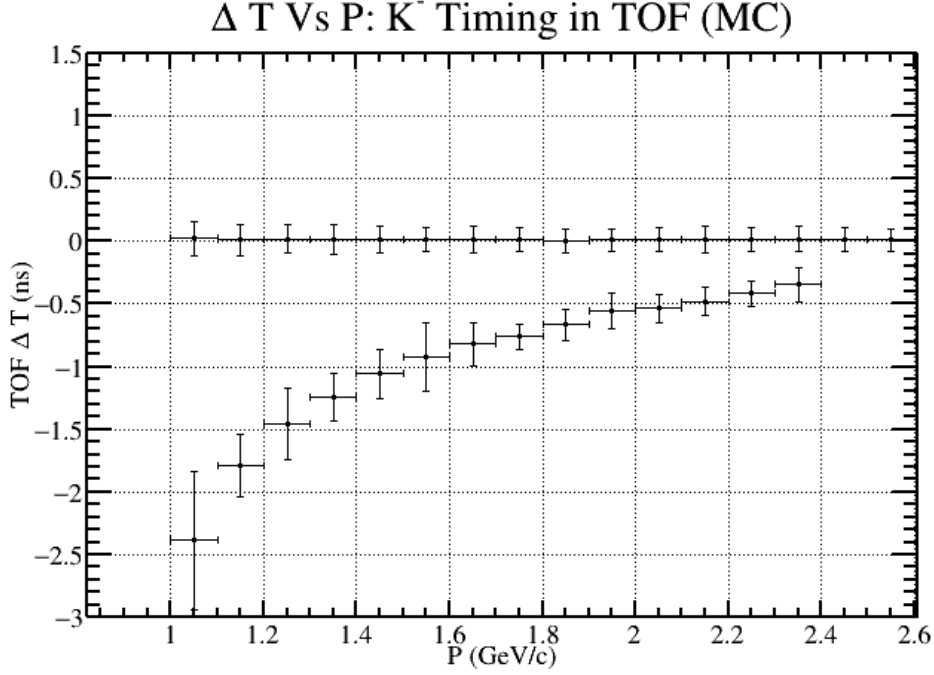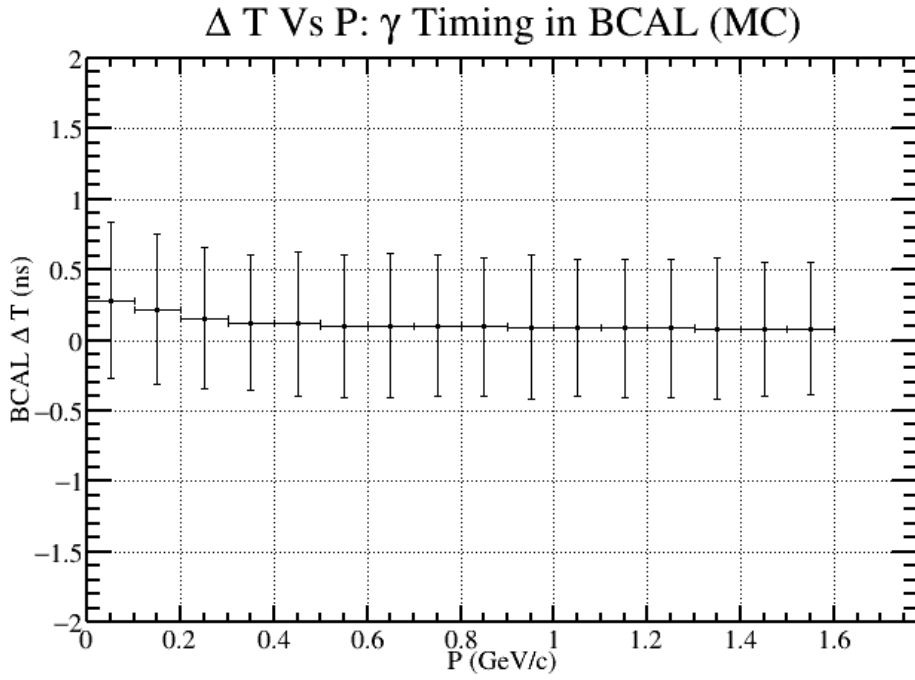
Figure 48: The image above is the result of the timing study performed on Figure [47]. Using that figure, a number of projection histograms were fit using different momentum ranges. The horizontal position of each point is in the middle of the projection range, and the vertical position of each point was assigned based on the mean value of the Gaussian fit. The horizontal error bars are the size of the projection range, which is always 0.1 GeV/c. The vertical error bars are determined by the width of the Gaussian fit. The average of the widths of the photon peaks is $\sim 0.5ns$ which is the value used to determine the timing cut in Table [1].
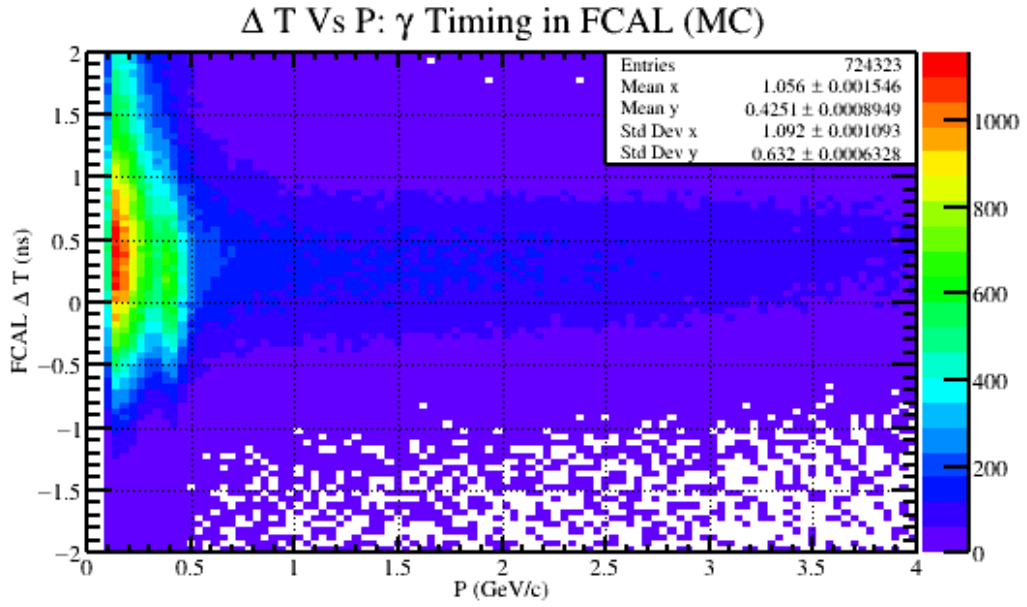
Figure 49: A timing plot for generated γ after reconstruction. The horizontal axis is the reconstructed momentum of the γ and the vertical axis is the timing difference between the FCAL and RF.
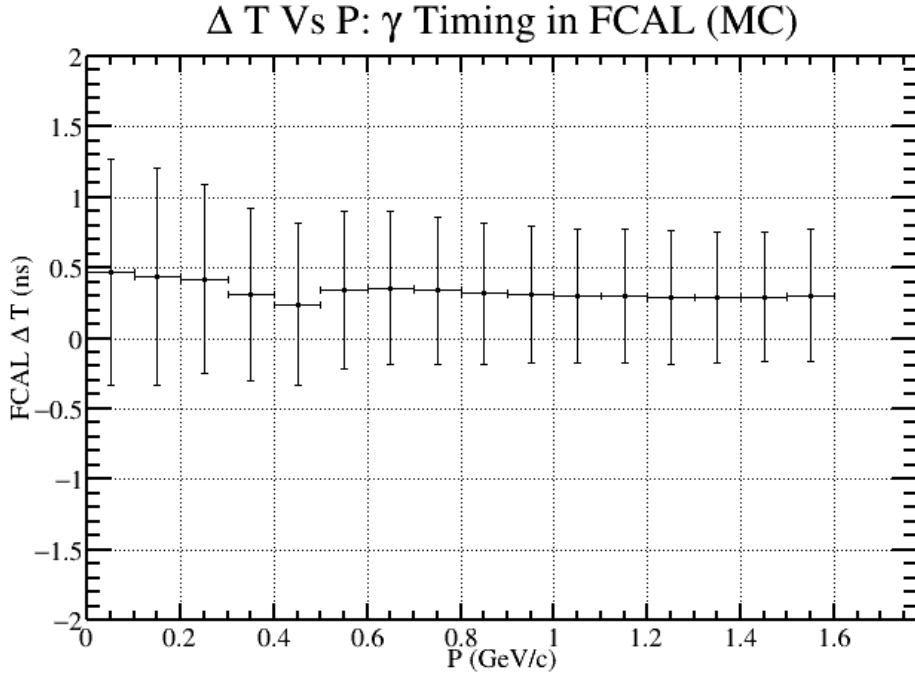
Figure 50: The image above is the result of the timing study performed on Figure [49]. Using that figure, a number of projection histograms were fit using different momentum ranges. The horizontal position of each point is in the middle of the projection range, and the vertical position of each point was assigned based on the mean value of the Gaussian fit. The horizontal error bars are the size of the projection range, which is always 0.1 GeV/c. The vertical error bars are determined by the width of the Gaussian fit. The average of the widths of the photon peaks is $\sim 0.55ns$ which is the value used to determine the timing cut in Table [1].
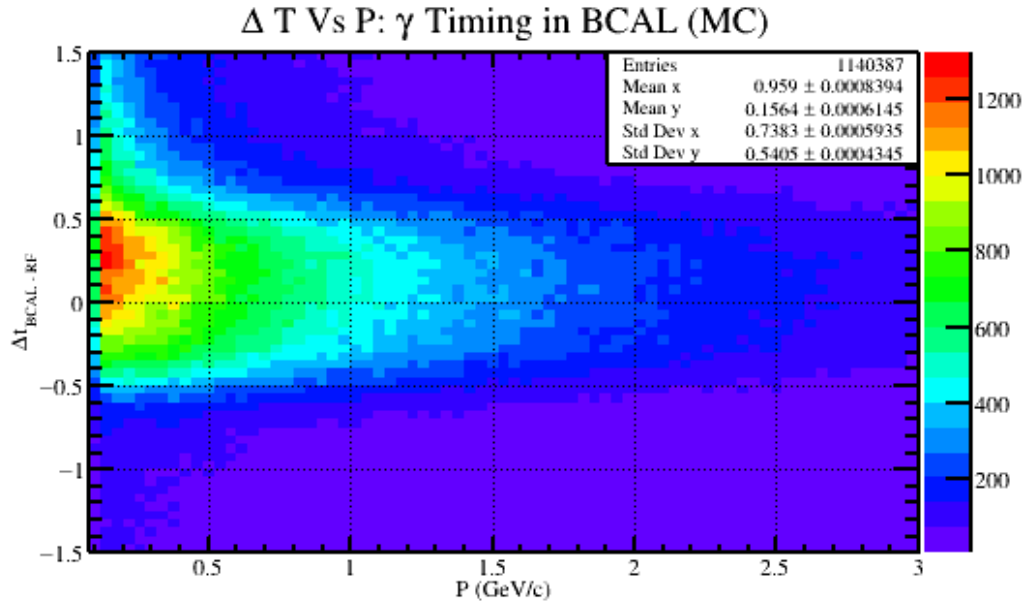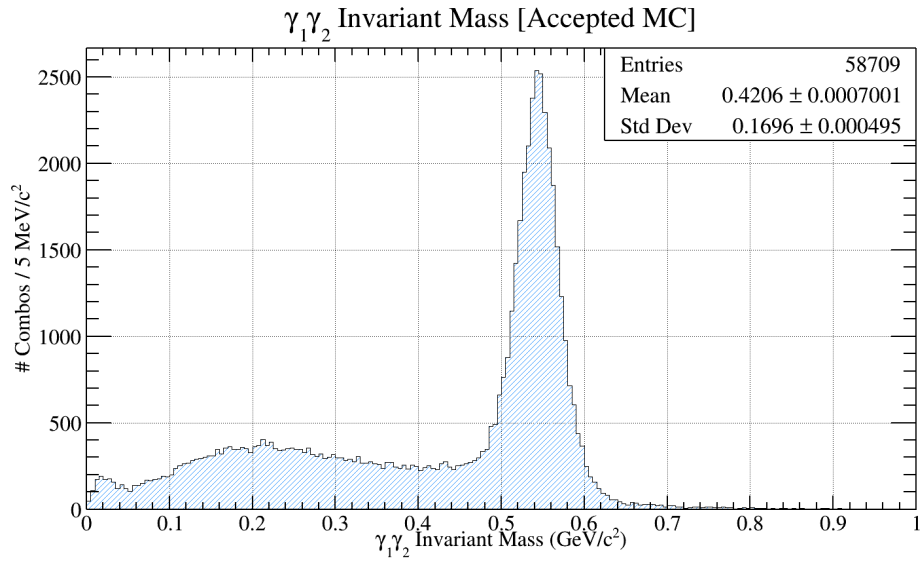
Figure 51: Invariant mass of the reconstructed $\gamma_1\gamma_2$ pair from accepted Monte Carlo. This Monte Carlo data originally came from a $\gamma p \rightarrow p\phi\eta; \phi \rightarrow K^+K^-; \eta \rightarrow \gamma\gamma$ generated topology. An interesting feature of this invariant mass spectra is that it shows a clear η peak, but also contains a background as well. The source of this background is thoroughly studied in subsection 3.3.
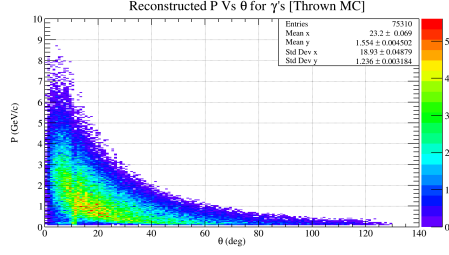
(a) P Vs θ distribution for thrown Monte Carlo photons.
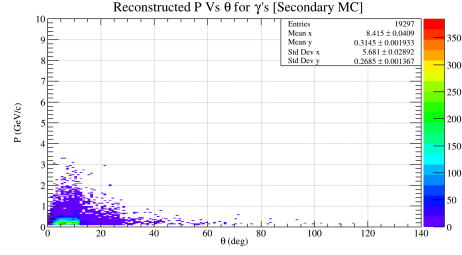
(b) P Vs θ distribution for secondary Monte Carlo photons.
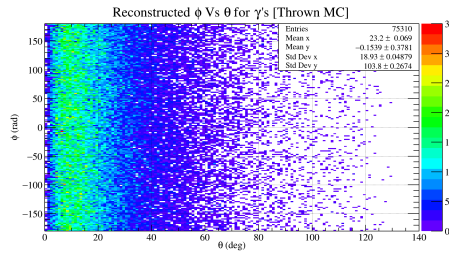
(c) ϕ Vs θ distribution for thrown Monte Carlo photons.
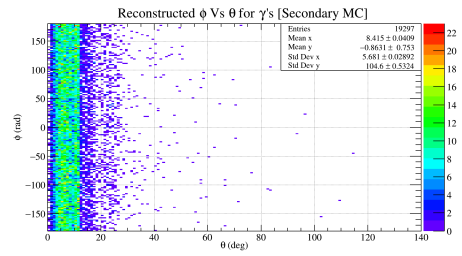
(d) ϕ Vs θ distribution for secondary Monte Carlo photons.

Figure 52: P Vs θ and ϕ Vs θ distributions for thrown (left column) and secondary (right column) photons inside accepted Monte Carlo data.
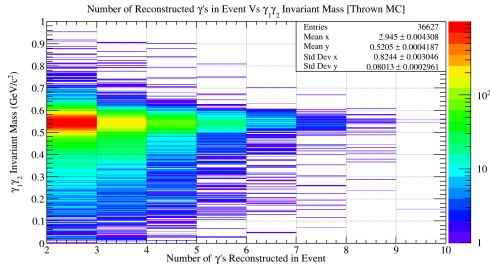
(a) Number of photons reconstructed in an event versus $\gamma_1\gamma_2$ Invariant Mass for thrown photons.
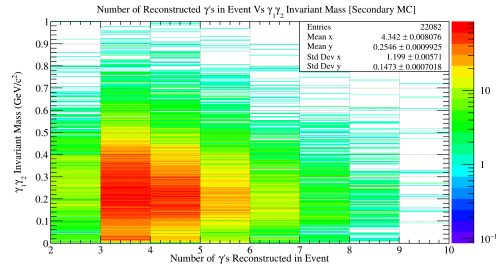
(b) Number of photons reconstructed in an event versus $\gamma_1\gamma_2$ Invariant Mass for secondary photons.

Figure 53: Comparing how the invariant mass for a given $\gamma\gamma$ pair changes depending on the number of reconstructed photons in an event and whether or not the photons were thrown or secondary photons.
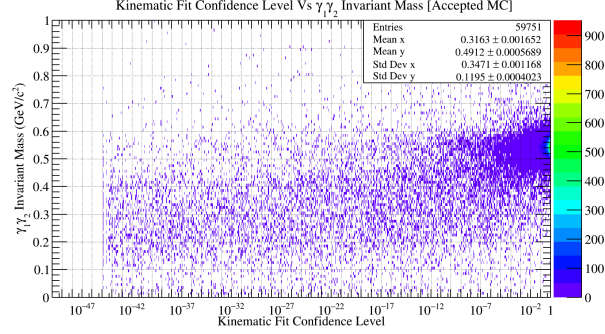
(a) Kinematic Fit confidence level (scaled logarithmically) versus $\gamma_1\gamma_2$ Invariant Mass for accepted Monte Carlo.

(b) Kinematic Fit confidence level (scaled logarithmically) versus $\gamma_1\gamma_2$ Invariant Mass for background generated Monte Carlo.
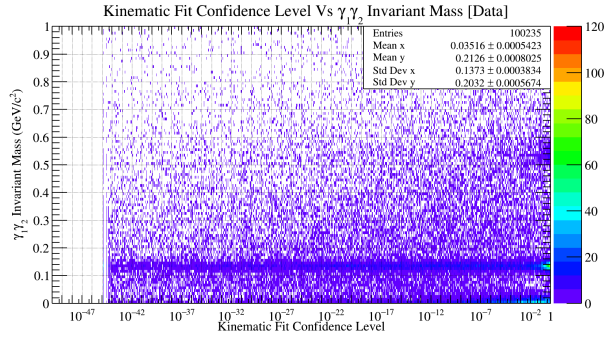
(c) Kinematic Fit confidence level (scaled logarithmically) versus $\gamma_1\gamma_2$ Invariant Mass for data.

Figure 54: Kinematic Fit confidence level (scaled logarithmically) versus $\gamma_1\gamma_2$ Invariant Mass for accepted Monte Carlo, background generated Monte Carlo, and data.
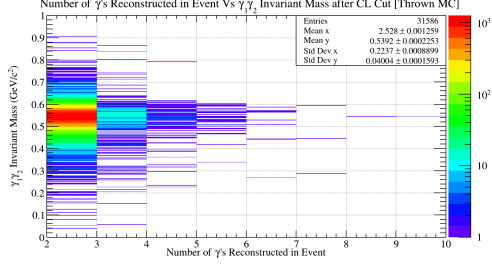
(a) Number of photons reconstructed in an event versus $\gamma_1\gamma_2$ Invariant Mass for thrown photons after a Kinematic Fit confidence level cut of $1x10^{-6}$.
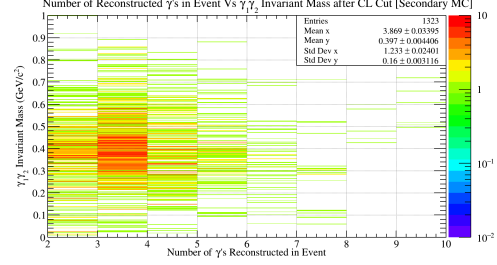
(b) Number of photons reconstructed in an event versus $\gamma_1\gamma_2$ Invariant Mass for secondary photons after a Kinematic Fit confidence level cut of $1x10^{-6}$.
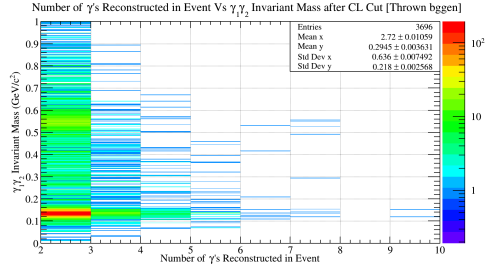
(c) Number of photons reconstructed in an event versus $\gamma_1\gamma_2$ Invariant Mass for thrown photons from `bggen` data after a Kinematic Fit confidence level cut of $1x10^{-6}$.
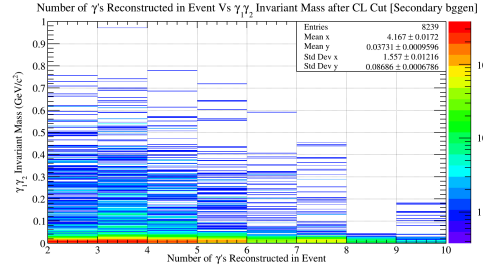
(d) Number of photons reconstructed in an event versus $\gamma_1\gamma_2$ Invariant Mass for secondary photons from `bggen` data after a Kinematic Fit confidence level cut of $1x10^{-6}$.
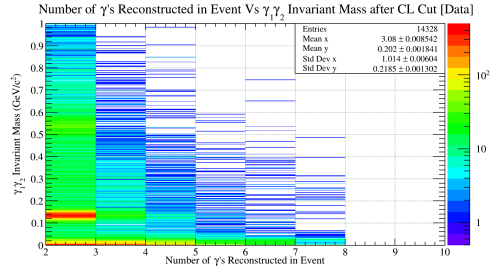
(e) Number of photons reconstructed in an event versus $\gamma_1\gamma_2$ Invariant Mass for data after a Kinematic Fit confidence level cut of $1x10^{-6}$.

Figure 55: Number of photons reconstructed in an event versus $\gamma_1\gamma_2$ Invariant Mass for accepted Monte Carlo, `bggen`, and data after a Kinematic Fit confidence level cut of $1x10^{-6}$.
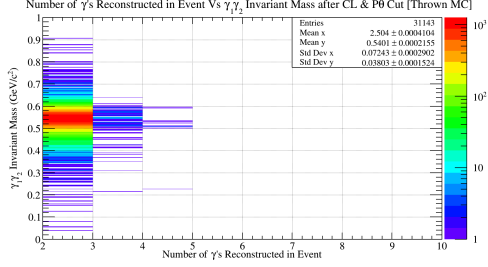
(a) Number of photons reconstructed in an event versus $\gamma_1\gamma_2$ Invariant Mass for thrown photons after a confidence level cut of $1x10^{-6}$ and a P Vs θ cut.
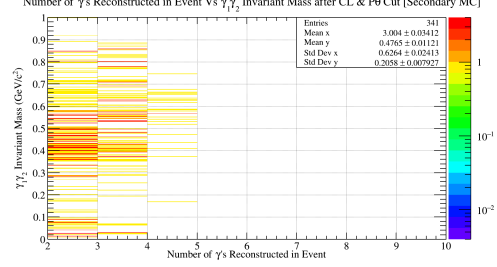
(b) Number of photons reconstructed in an event versus $\gamma_1\gamma_2$ Invariant Mass for secondary photons after a confidence level cut of $1x10^{-6}$ and a P Vs θ cut.
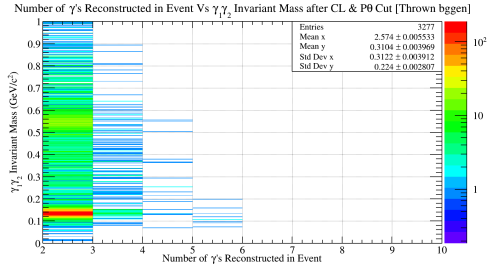
(c) Number of photons reconstructed in an event versus $\gamma_1\gamma_2$ Invariant Mass for thrown photons from `bggen` data after a confidence level cut of $1x10^{-6}$ and a P Vs θ cut.
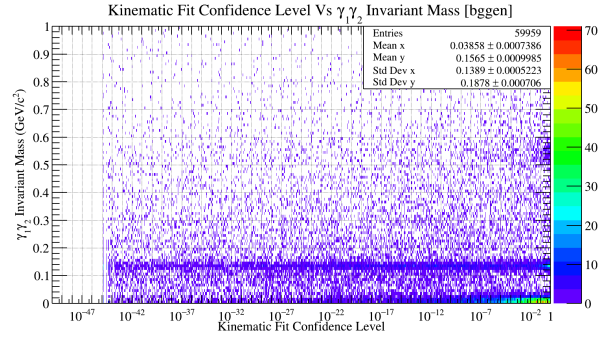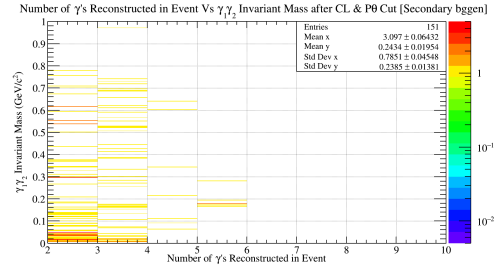

(d) Number of photons reconstructed in an event versus $\gamma_1\gamma_2$ Invariant Mass for secondary photons from `bggen` data after a confidence level cut of $1x10^{-6}$ and a P Vs θ cut.
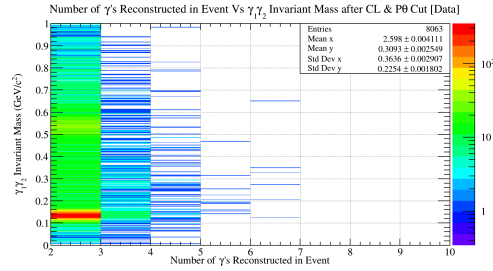
(e) Number of photons reconstructed in an event versus $\gamma_1\gamma_2$ Invariant Mass for data after a confidence level cut of $1x10^{-6}$ and a P Vs θ cut.

Figure 56: Number of photons reconstructed in an event versus $\gamma_1\gamma_2$ Invariant Mass for accepted Monte Carlo, `bggen`, and data after a confidence level cut of $1x10^{-6}$ and a P Vs θ cut.

60

4 Probabilistic Weightings for $\phi\eta$ Events

Throughout the course of history, physicists have tried clever ways of reducing the amount of background that is present under a given signal, or resonance. An example of this may be the classic side band subtraction, where the signal region will be defined by some average mass value, plus or minus a well defined width, or sigma. If one were to perform a cut about this region after particle identification and cuts, there may still be a good deal of background underneath the peak. In order to eliminated the background under the signal, one thing to do is use the background near the peak as reference for subtraction. To do this, one would use background events that are located at both higher and lower mass values far away from the signal, so long as the total mass range used is equal to the mass range for selecting the signal region. The side band subtraction method works well in practice, but does not necessarily model the background accurately near or around the signal. In fact, it is better to use the side band subtraction method when a resonance has a linear background, or a background that is understood well enough to justify the method. Unfortunately for the $\phi\eta$ final state, this is not the case.

One reason that this cannot be done is the simple fact that the ϕ meson has a non linear background due to the fact that it is so close in mass to the K^+K^- threshold. This dynamically changing background effectively eliminates the side band subtraction method due to the difference in statistics for low and high K^+K^- mass values relative the the ϕ peak. Furthermore, the background underneath the ϕ peak is not well understood for the GlueX experiment, and therefore an attempt at modeling this behavior is not possible either. Lastly, performing a side band subtraction on the ϕ does not definitively help to select the $\phi\eta$ final state. Therefore, a better method may involve doing a two dimensional 'box' cut about the ϕ and η mass values. In principle, this is exactly the same method as before, only in two dimensions; where the width of the box would be proportional to the width of ϕ meson, and the height of the box would be proportional to the width of η meson. However, this method is not a wise choice for two reasons. One of which is the fact that performing a box cut actually injects more background into your signal region. This is due to the fact that, roughly speaking, the ϕ and η masses are Gaussian in shape. The intersection of two Gaussian shaped resonances in two dimensions will create a topology which is more elliptical in shape, rather than rectangular in shape. Attempting a box cut selection on the signal region in two dimensions would induce extra backgrounds near the corners of the box due to the elliptical shape of the $\phi\eta$ intersection. The second reason that a box cut is not a good idea relates back to the one dimen-

sional argument about the background under the ϕ peak. The only difference now is that the analysis would have to justify that the background in two dimensions is well understood, rather than just one. This argument would not only apply to a box cut method, but *any* two dimensional geometric shape, including an ellipse. Therefore, this thesis will not consider any side band background subtraction method, in any dimension.

4.1 Introduction to Probabilistic Event Weightings

The underlying issue with all of the background subtraction methods above is that they treat all events with a relative weight of one. The purpose of this section is to describe and propose a new method which does not treat all events with a value of one, but instead assigns a fractional weight to an event based off of a quality factor, or Q-factor. The quality value idea was first introduced in 2008 by M. Williams, M. Bellis, and C. A. Meyer in a paper titled *"Separating Signals from Non-Interfering Backgrounds using Probabilistic Event Weightings."*. The paper considers a generic situation in which there is a data set of n total events described by m coordinates, which will be written as $\vec{\xi}$. Within the data set, there exists n_s total signal events and n_b total background events, and therefore $n = n_s + n_b$. In addition, both the signal and the background distributions are functions of the coordinates, such that $S(\vec{\xi})$ can be thought of as a signal distribution and $B(\vec{\xi})$ can be thought of as a background distribution. Contained within the set of coordinates $\vec{\xi}$, there exists a *reference coordinate* ($\vec{\xi}_r$) with which we know the functional form of $S(\vec{\xi})$ and $B(\vec{\xi})$ *a priori*. The reference coordinate that is used in this thesis as well as in the paper mentioned above is the invariant mass of a final state. For many invariant mass distributions, the functional form of the signal distribution, $S(\vec{\xi})$ can be represented with some function; typically a Gaussian, or in the case of this thesis, a Voigtian. In addition, the background distribution, $B(\vec{\xi})$, can be represented with a polynomial function.

Since the signal and background distributions are not necessarily known *a priori* for the other coordinates, we use them to calculate a kinematic distance on an event by event basis. This is done by using the Equation (1).

$$d_{ij}^2 = \sum_{k \neq r} \left[\frac{\xi_k^i - \xi_k^j}{R_k} \right]^2 \tag{1}$$

In Equation(1), the total kinematic distance is calculated between some event i, as compared to another event j. This is done by taking the sum of the squared difference over all of the coordinates ξ_k, except for the reference

coordinate ξ_r. The difference between coordinates is then normalized by the parameter R_k. The parameter R_k is the total maximum difference for a given coordinate ξ_k. An example of this may be the measurement of an azimuthal angle which spans from 0 to 2π. Therefore, the R_k for an azimuthal angle would be 2π. Upon closer inspection, one should realize that Equation(1) is simply a representation of the Pythagorean Theorem in a normalized $m-1$ dimensional kinematic space.

After calculating all of the kinematic distances for an event i, as compared to all other events within the data set $1...j...n$, it is then necessary to only keep the *nearest neighbors*. The nearest neighbors, by definition, are a subset of the n events which have the smallest kinematic distance with respect to the ith event that you are considering. The purpose of only keeping the nearest neighbors stems from the assumption that a signal or background event with certain kinematic measurements will share similar values with other signal or background events, respectively. The number of nearest neighbors for a set of events n is an arbitrary amount, and does not greatly effect the quality factor calculation; so long as the amount is some fraction of the total events n. Once the list of nearest neighbors is known for the ith event, it is then necessary to plot their reference coordinate, ξ_r, onto a histogram. This histogram should contain a well understood signal distribution $S(\xi_r, \vec{\alpha})$, and background distribution $B(\xi_r, \vec{\alpha})$, as mentioned above; where $\vec{\alpha}$ is the set of unknown fit parameters used to describe the signal or background distribution. The histogram will then be fit by the sum of the signal and background distributions such that $F(\xi_r, \vec{\alpha}) = S(\xi_r, \vec{\alpha}) + B(\xi_r, \vec{\alpha})$. The quality factor can then be calculated by using the reference coordinate value for the ith event and plugging it into the signal and background functions by using Equation(2), where $\hat{\alpha}$ is the set of fitted parameters for the signal or background distribution.

$$Q_i = \frac{S(\xi_r^i, \hat{\alpha}_i)}{S(\xi_r^i, \hat{\alpha}_i) + B(\xi_r^i, \hat{\alpha}_i)} \tag{2}$$

Once the quality factor is known for an event i, it can then be recorded and the analysis can loop over the next event and repeat the sequence all over again. Once all events have been run over, the quality factors for each event are used as a weight for plotting inside histograms. If the quality factor is correctly calculated for each event, the method should be able to separate signal from background. More specifically, if a histogram of the K^+K^- invariant mass is plotted with Q_i as the weight for the ith event, one should see a 'pure' ϕ peak with absolutely no background. In addition, if the K^+K^- invariant mass is plotted with $1 - Q_i$ as the weight for the ith event, one should see all background and absolutley no ϕ peak. Therefore, the sum

of the signal histogram plus the background histogram should be equal to the non weighted K^+K^- invariant mass which will include both signal and background events.

4.2 Example of $\phi\eta$ Quality Factor Method

All of the content mentioned above is a general description of the quality factor calculation for any physics analysis. However, it does not specifically address the method used by this thesis which ultimately aims to observe a $\phi\eta$ final state. In order to properly identify $\phi\eta$ events, a double quality factor calculation was performed on the data after selection cuts. This means that both the K^+K^- invariant mass and the $\gamma_1\gamma_2$ invariant mass were fitted for each event. After fitting, a quality factor was calculated for the K^+K^- invariant mass, and a separate quality factor was calculated for the $\gamma_1\gamma_2$ invariant mass. Once both quality factors were calculated, a total quality factor was assigned to the overall event by multiplying the ϕ and η quality factors together. The total quality factor is then used as the final weight for plotting each event in the final analysis of this thesis. This subsection will go into great detail as to how this quality factor calculation was performed.

4.2.1 Calculating the Kinematic Distance Between Events

Since it is in our interest to observe the $\phi\eta$ final state, the coordinates to be used in the calculation for the kinematic distance between events (Equation 1) should be a set which can describe the entire reaction. In order to describe the $\gamma p \rightarrow p\phi\eta$; $\phi \rightarrow K^+K^-$; $\eta \rightarrow \gamma\gamma$ final state, there are a total of eight observables, or coordinates needed. Four of the eight coordinates come from the angular distributions of the daughter states of ϕ and η. More specifically, the four coordinates are $K^+_{HE\cos(\theta)}$, $K^+_{HE\phi}$, $\gamma_{HE\cos(\theta)}$, $\gamma_{HE\phi}$; where the angles ϕ and θ are the polar coordinates in the helicity reference frame. It should be noted that since the K^+ and γ particles are daughters of different parent states, they will have different helicity frames which are relative to the rest frames of ϕ and η, respectively. Two more of the eight total coordinates will come from the angular distributions of ϕ and η. Much like the K^+ and γ particles, these coordinates will be $\phi_{GJ\cos(\theta)}$ and $\phi_{GJ\phi}$; where ϕ and $\cos(\theta)$ are polar angles in the Gottfried-Jackson frame; or the rest frame of the $\phi\eta$ parent state. The last two coordinates needed to describe the $\gamma p \rightarrow p\phi\eta$ final state is the beam energy (γ_E), and the momentum transfer, t. Since t is the well known Mandelstam variable, t is related to the beam energy and the four momentum of the $\phi\eta$ parent state, such that $t^2 = (\gamma^\mu - X^\mu)^2$; where γ^μ is the energy-momentum four vector for the beam, and X^μ is the energy-

momentum four vector for the $\phi\eta$ parent state. Since t, the beam energy γ_E, and the mass of the $\phi\eta$ parent state is known, the magnitude of the $\phi\eta$ parent state momentum is directly proportional to these measurements. Knowing the magnitude of the momentum and the mass of the $\phi\eta$ parent state allows us to fully describe the $\gamma p \to p\phi\eta$ reaction. The final detail that needs to be mentioned is the reference coordinates that are used in this quality factor analysis. Because it is imperative to have a pure ϕ and η signal, there will be two reference coordinates for this procedure. One of them will be the K^+K^- invariant mass, and the other will be the $\gamma_1\gamma_2$ invariant mass. Although these coordinates do not play a role in the calculation of the kinematic distance, it is imperative to define them as the reference coordinates which will ultimately serve as the tool to separate signal events from background events. A table which summarizes the coodinates used to calculate the kinematic distance between events is given in Table 2 below.

ξ_k	Coordinate	Maximum Range of Coordinate
ξ_0	$K^+_{HE\cos(\theta)}$	2
ξ_1	$K^+_{HE\phi}$	2π radians
ξ_2	$\gamma_{HE\cos(\theta)}$	2
ξ_3	$\gamma_{HE\phi}$	2π radians
ξ_4	$\phi_{GJ\cos(\theta)}$	2
ξ_5	$\phi_{GJ\phi}$	2π radians
ξ_6	γ_E	4 GeV
ξ_7	t	$3.3\dfrac{GeV^2}{c^4}$
ξ_r	K^+K^- Invariant Mass	Reference Coordinate
ξ_r	$\gamma_1\gamma_2$ Invariant Mass	Reference Coordinate

Table 2: A table which summarizes the coordinates used to describe the $\gamma p \to p\phi\eta$; $\phi \to K^+K^-$; $\eta \to \gamma\gamma$ final state. The coordinates ξ_0 through ξ_7 are used in the kinematic distance equation, described by Equation (1). The last two coordinates are the reference coordinates for this analysis.

4.2.2 Determining the Number of Nearest Neighbors

After the kinematic distances are calculated for all events with respect to the ith event, they are the sorted in order from smallest kinematic distance to largest kinematic distance. Only the the nearest neighbors, or the set of events with the smallest kinematic distance, will be used to determine the quality factor of a given event. For this analysis, there were a total of

108,617 events after selection cuts., and the number of nearest neighbors used was 3,000. This number was chosen somewhat arbitrarily; it is important to pick the smallest number possible such that the events used truly are those which share the most similar kinematic features to the event that is being considering. If the number was extremely large with respect to the total number of events, the analysis will not work properly. Events that are background will have some nearest neighbors that are signal, and vice versa. Furthermore, the number number of nearest neighbors needs to be large enough such that a fit can be converged with the filled histogram. If the number of nearest neighbors is too small, ROOT will fail to provide any signal or background information inside the histogram, and therefore calculation of a quality factor will be impossible. Considering these two constraints and testing with different values, it was found that the smallest number which did not result in *any* fitting failures was 3,000.

4.2.3 Fitting the K^+K^- Invariant Mass

Upon determining the nearest neighbors of the ith event, the next step is to plot and fit the set of K^+K^- and $\gamma_1\gamma_2$ invariant mass distributions. As mentioned above, it is extremely difficult to model the invariant mass distribution for the K^+K^- final state. Simply picking a signal distribution plus a polynomial background is not enough to properly parameterize the K^+K^- invariant mass near or around the ϕ peak. After attempting several different combinations of signal and background functions, it was found that the best way to accurately describe both the ϕ and the background near it is to use convoluted functions. A convolution is the operation between two functions which expresses how the shape of one function is modified by the other. The purpose for utilizing a convoluted function when attempting to fit an invariant mass histogram is to describe both the shape of the distribution as well as the inherent resolution of the data. Since both the ϕ peak and the background surrounding it contain similar resolutions, it is appropriate to fit the K^+K^- invariant mass distribution with the summation of a signal function plus a background function, both of which are then convoluted by a third function which manages the resolution.

The signal function chosen to fit describe the ϕ peak is a relativistic Breit-Wigner. Since the ϕ peak is close to the K^+K^- threshold, it is important to consider the effect of a mass dependent width, which can be distorted due to rapidly changing breakup momentum. Contained within the relativistic Breit-Wigner are two free parameters and one independent variable. One of the free parameters is the amplitude which simply controls the height of the resonance, and the other is the ϕ mass. Although the mass is technically

a free parameter, due to experimental and statistical resolutions, it is still tightly restricted and therefore forced to be close to the ϕ mass provided by the PDG (Table 3). Lastly, the independent variable for the relativistic Breit-Wigner is simply the K^+K^- invariant mass. Plotted along with the signal function is the background function which is simply a third degree polynomial, which is given in Equation (3).

$$b(x) = C_1 * (x - C_0)^3 + C_2 * (x - C_0)^2 + C_3 * (x - C_0) \tag{3}$$

The background equation has three free parameters and one fixed parameter, as well as one independent variable which is once again the K^+K^- invariant mass. The free parameters are the coeffcients in front of the powered terms of x, specifically C_1, C_2, and C_3. Since the background shape can drastically change due to the event and its nearest neighbors, these parameters are not given any restriction on their values (Table 3). The one fixed parameter is C_0 which is set to $0.987354\dfrac{GeV}{c^2}$. This value is the smallest possible mass which can produce the K^+K^- final state, and is easily derived by simply performing the calculation $m_{K^+} + m_{K^-} = 2 * m_{K^\pm} = 0.987354\dfrac{GeV}{c^2}$. The purpose of fixing this parameter is force the polynomial background to have a root at the K^+K^- threshold. While attempting different fit functions to describe the K^+K^- invariant mass, it was found that the polynomial function often exaggerated, or over fit the area near the K^+K^- threshold. This caused an effect which resulted in weighted histograms that took away good events near the low mass side of the ϕ peak. Forcing the background function to be equal to zero at the K^+K^- threshold fixed this issue.

Lastly, the signal and background function are added together, then convoluted by a Gaussian in order to compensate for the resolution of the GlueX spectrometer. Although the signal and background functions mentioned above had to be programmed by hand, the convolution of these functions with a Gaussian could be fed into the ROOT library using the TF1Convolution object. More precisely, the total function used to describe the K^+K^- invariant mass for all events is given in Equation (4).

$$T(x) = \int \left[s(x') + b(x')\right] G(x - x') dx' \tag{4}$$

In the equation above, x' is simply a dummy variable for integration, and x represents the K^+K^- invariant mass. The function $s(x')$ is a relativistic Breit-Wigner, and the $b(x')$ is the polynomial background function referenced in Equation (3). Finally, $G(x - x')$ is the Gaussian function which is responsible for describing the resolution. This particular Gaussian function

has one free parameter, one fixed parameter, and one independent variable. The free parameter is the width of the Gaussian, and the fixed parameter is the mean of the Gaussian which is simply set to zero. Because the Gaussian is being convoluted over the range of the fit, the value of the mean in this instance does not matter. Adding all things together, the total function listed in Equation (4) has one independent variable, two fixed parameters, and six free parameters, half of which are restricted (Table 3). Once a fit has converged, the parameters of the total function can be extracted and used to plot a signal function and a background function. This procedure is mathematically allowed due to the distributive property of convolutions; and therefore the final background and signal function can be written in Equation (5) and Equation (6), respectively.

$$B(x) = \int b(x')G(x - x')dx' \tag{5}$$

$$S(x) = \int s(x')G(x - x')dx' \tag{6}$$

Examples of different fits of the K^+K^- invariant mass distributions have been provided in Figures[57][58][59]. Each figure contains a blue line which represents the total fit of the data (Equation 4), a green line which represents the signal portion of the fit (Equation 6), and a red line which represents the background portion of the fit (Equation 5). Located within each plot is also a vertical arrow which is pointed in the downward direction. This arrow represents the invariant mass value of the event for which the quality factor is being calculated. Also contained within each figure is a legend with the values of the parameters for each fit.

4.2.4   Fitting the $\gamma_1\gamma_2$ Invariant Mass

On top of fitting the K^+K^- invariant mass, it is also necessary to fit the $\gamma_1\gamma_2$ invariant mass. Fitting this distribution is far more simple than what was needed to describe the K^+K^- invariant mass. For the most part, the η resonance sits on top of a relatively linear background, and is far enough away from the dominant π^0 peak that further inspection of the background is not necessary. In addition, since the η resonance is nowhere near the threshold for $\gamma\gamma$, performing any type of advanced fit to include breakup momentum and resolution effect is not necessary. Therefore, the $\gamma_1\gamma_2$ invariant mass spectra was fit by utilizing the summation of a signal function and a background function. The signal function is a Voigtian, which is technically a non relativistic Breit-Wigner convoluted with a Gaussian. This convolution

68

temp_hist

Entries		3000
Mean		1.138 ± 0.001912
Std Dev		0.1047 ± 0.001352
Amplitude		108.7 ± 7.1
Phi Mass		1.02 ± 0.00
Threshold		0.9874 ± 0.0000
p1		2547 ± 353.1
p2		-1873 ± 160.8
p3		345.9 ± 17.6
Resolution		0.004275 ± 0.000550

Figure 57: A fit which will result in an extremely low quality factor due to the very few signal events in comparison to background events at the location of the arrow, or invariant mass of the event being considered.

temp_hist

Entries	3000
Mean	1.155 ± 0.00211
Std Dev	0.1156 ± 0.001492
Amplitude	78.69 ± 7.11
Phi Mass	1.022 ± 0.001
Threshold	0.9874 ± 0.0000
p1	4359 ± 409.6
p2	−2453 ± 179.9
p3	378.3 ± 19.0
Resolution	0.00656 ± 0.00107

Figure 58: A fit which will result in a quality factor around 0.5, due to the fact that there are roughly the same signal and background events at the location of the arrow, or invariant mass of the event being considered.

70

temp_hist

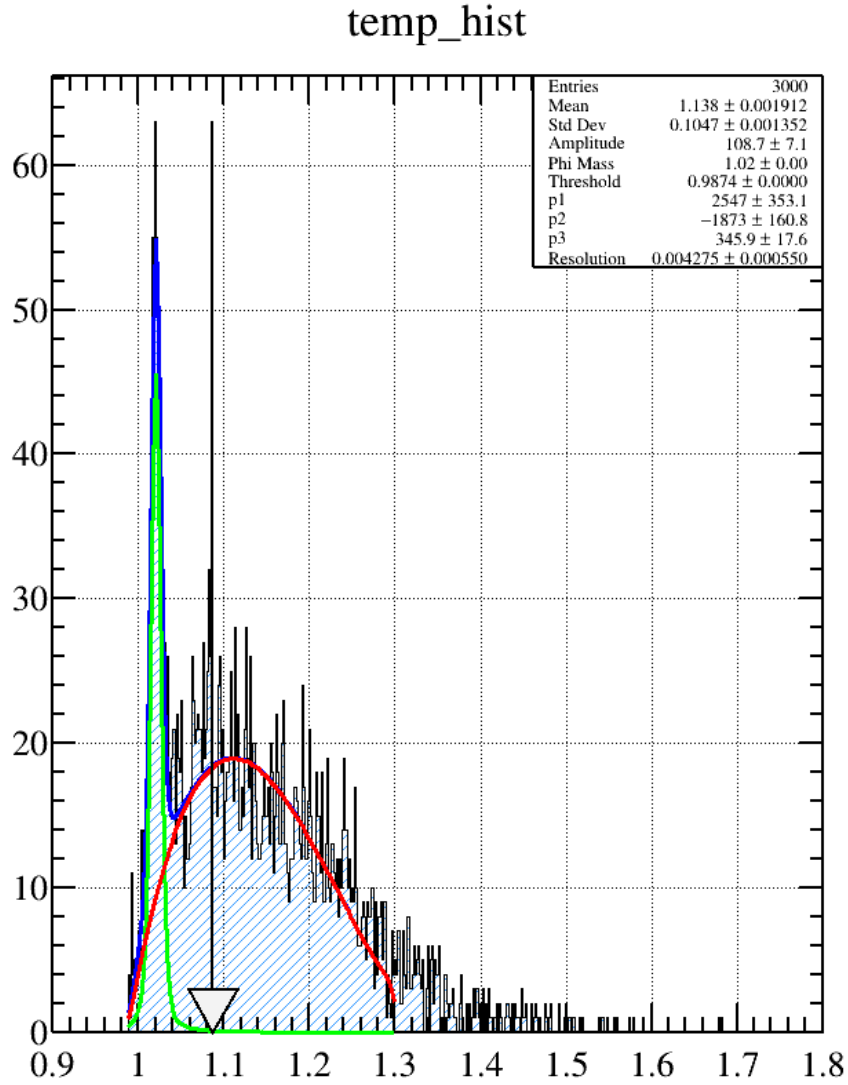| Entries	3000
Mean	1.107 ± 0.001949
Std Dev	0.1067 ± 0.001378
Amplitude	232.8 ± 9.7
Phi Mass	1.02 ± 0.00
Threshold	0.9874 ± 0.0000
p1	4790 ± 338.0
p2	−2680 ± 155.9
p3	386.3 ± 17.5
Resolution	0.006393 ± 0.000541

Figure 59: A fit which will result in a very high quality factor due to the large number signal events in comparison to background events at the location of the arrow, or invariant mass of the event being considered.
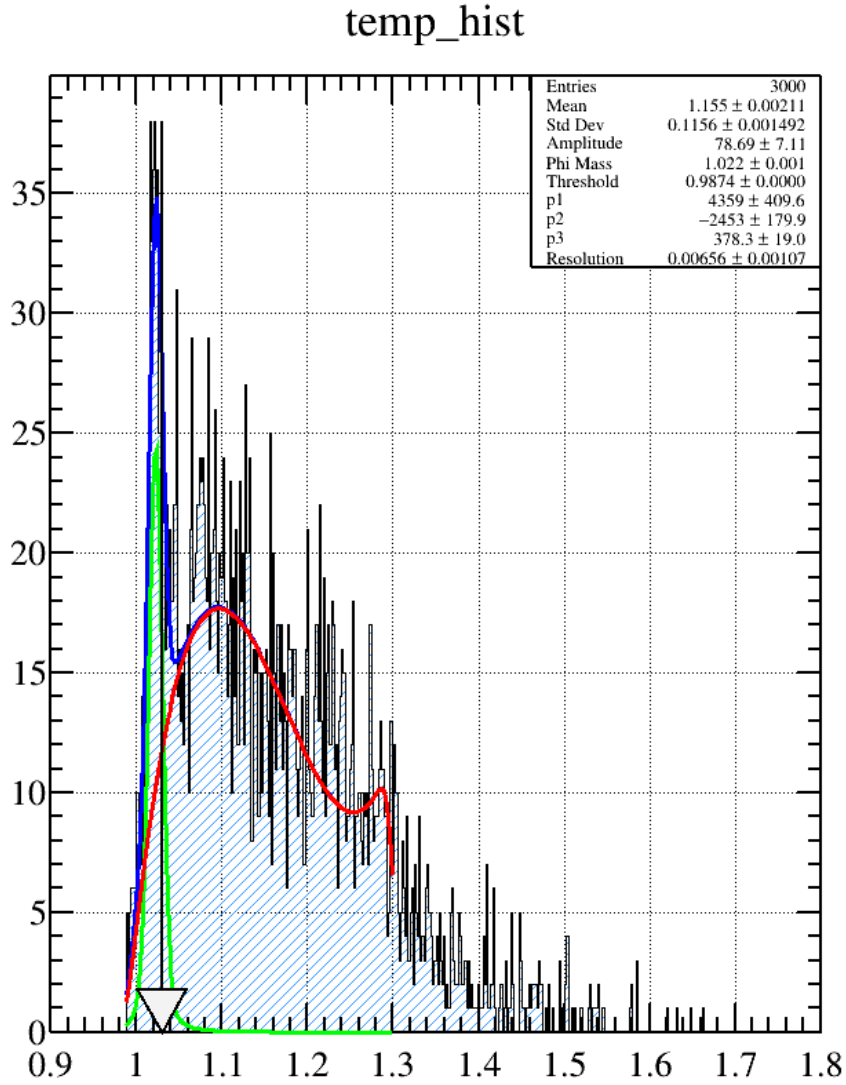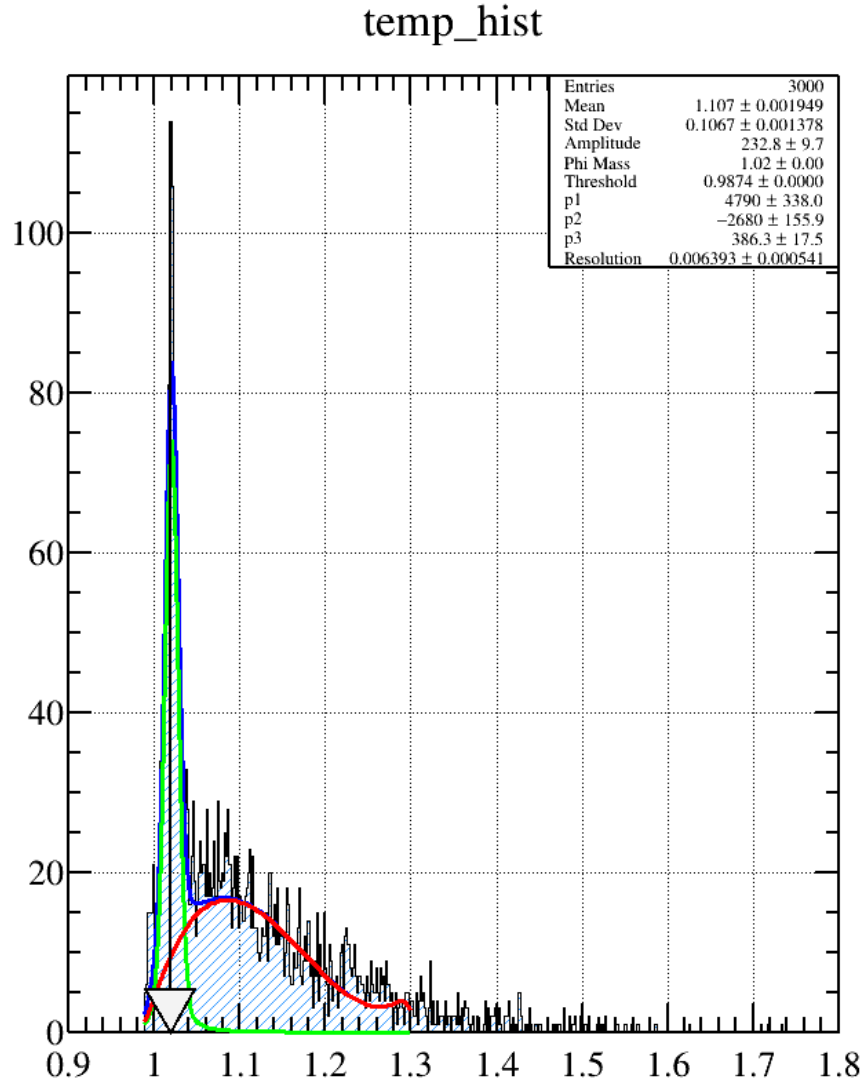
is necessary because the resolution of the η resonance is much greater than the natural width of the η meson, which is on the order of a keV. To make things simpler, the background function chosen was once again a third order polynomial. However, the functional form of this third order polynomial is different than the one that was used to describe the K^+K^- because there is no threshold effect that has to be accounted for in the $\gamma_1\gamma_2$ invariant mass. A review of all parameters and functions used to fit the K^+K^- invariant mass, as well as the $\gamma_1\gamma_2$ invariant mass is given in Table 3.

Examples of different fits of the $\gamma_1\gamma_2$ invariant mass distributions have been provided in Figures[60][61][62]. Just like the examples given for the K^+K^- invariant mass fits, each figure contains a blue line which represents the total fit of the data. The total fit in this particular instance is simply the sum of a Voigtian and a third degree polynomial. The figures also contain a green line which represents the signal portion of the fit and a red line which represents the background portion of the fit. These are described by a Voigtian and third degree polynomial, respectively. Located within each plot is also a vertical arrow which is pointed in the downward direction. This arrow represents the invariant mass value of the event for which the quality factor is being calculated. Also contained within each figure is a legend with the values of the parameters for each fit.

K^+K^- Invariant Mass Functions:

Function	Parameters	Initial Values	Restricted Range
Relativistic B.W.	Amplitude	10	$0-1000$
	m_ϕ	1.019	$1.01-1.03$
3rd Degree Polynomial	C_0	0.987354	Fixed
	C_1, C_2, C_3	$1500, -1200, 200$	Free
Gaussian	μ	0	Fixed
	σ	0.005	$0-0.05$

$\gamma_1\gamma_2$ Invariant Mass Functions:

Function	Parameters	Initial Values	Restricted Range
Voigtian	Amplitude	2	$0-5$
	m_η	0.547	$0.52-0.56$
	σ	0.02	$0.001-0.1$
	Γ	0.00000131	Fixed
3rd Degree Polynomial	C_0, C_1, C_2, C_3	None	Free

Table 3: A table which summarizes the parameters and functions used to fit the K^+K^- and $\gamma_1\gamma_2$ invariant mass histograms.

temp_hist_eta

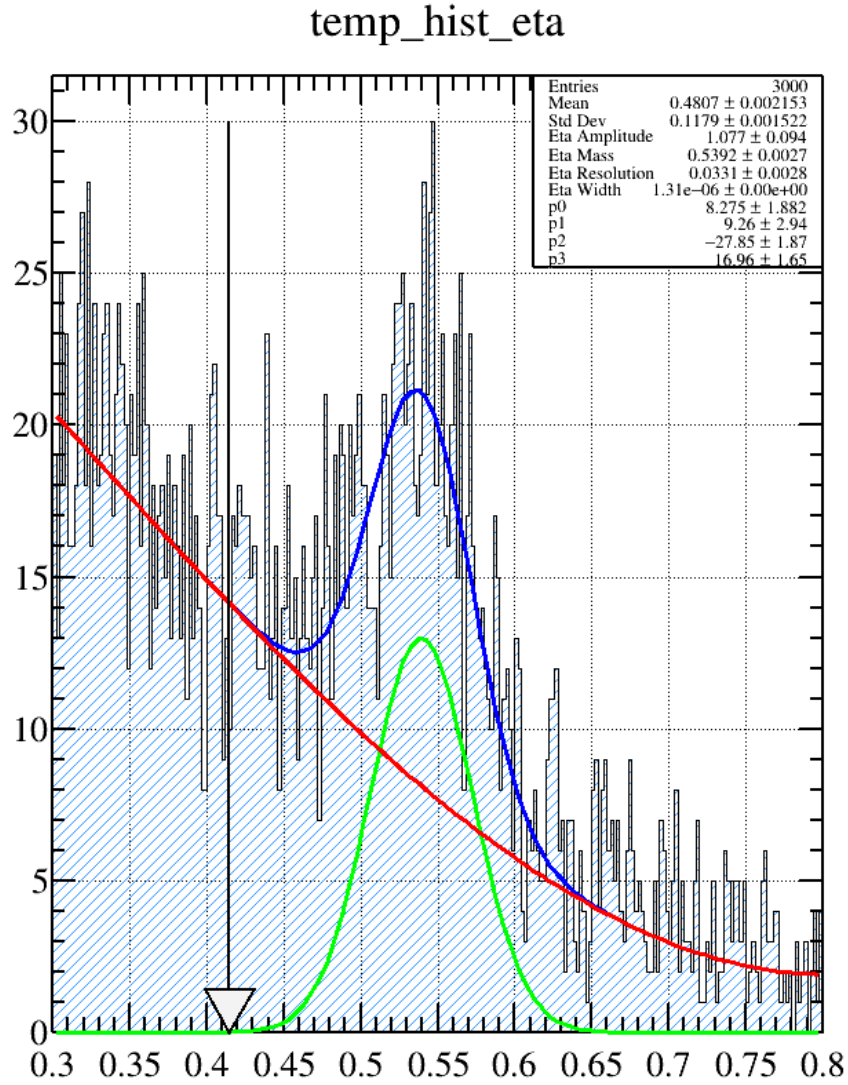| Entries	3000
Mean	0.4807 ± 0.002153
Std Dev	0.1179 ± 0.001522
Eta Amplitude	1.077 ± 0.094
Eta Mass	0.5392 ± 0.0027
Eta Resolution	0.0331 ± 0.0028
Eta Width	1.31e−06 ± 0.00e+00
p0	8.275 ± 1.882
p1	9.26 ± 2.94
p2	−27.85 ± 1.87
p3	16.96 ± 1.65

Figure 60: A fit which will result in an extremely low quality factor due to the very few signal events in comparison to background events at the location of the arrow, or invariant mass of the event being considered.

temp_hist_eta

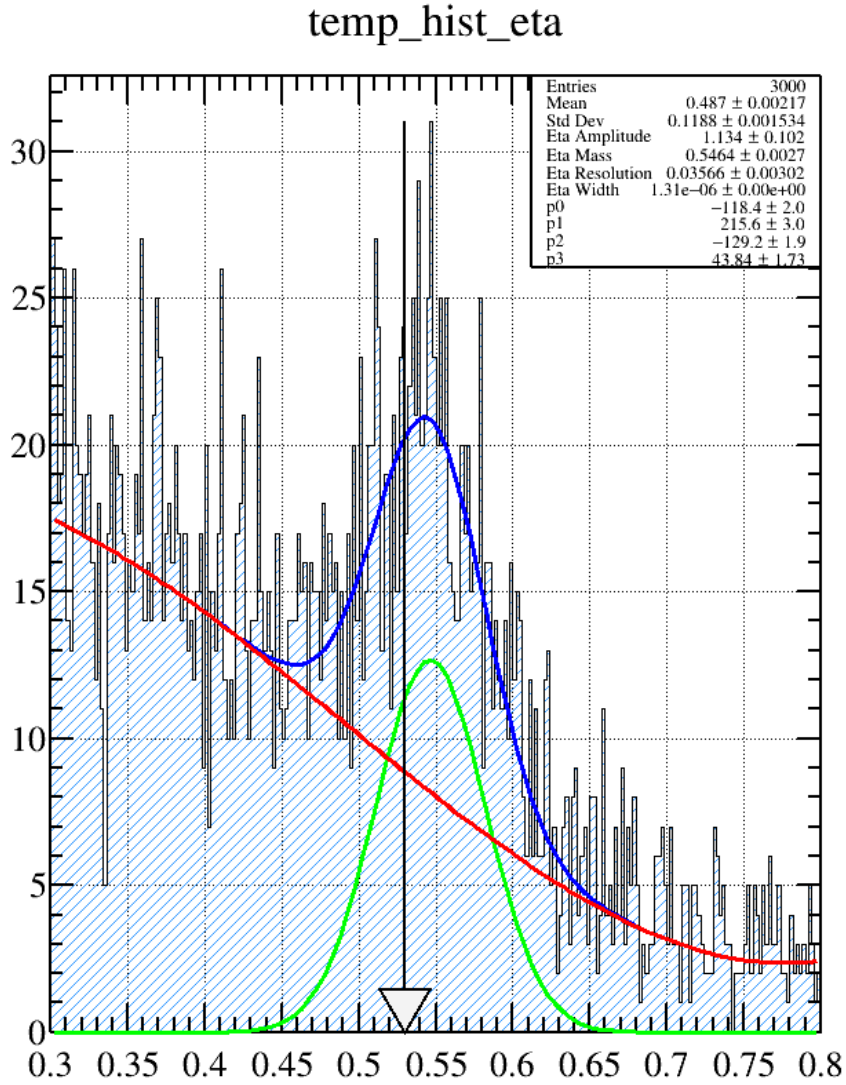|	
Entries	3000
Mean	0.487 ± 0.00217
Std Dev	0.1188 ± 0.001534
Eta Amplitude	1.134 ± 0.102
Eta Mass	0.5464 ± 0.0027
Eta Resolution	0.03566 ± 0.00302
Eta Width	$1.31e{-}06 \pm 0.00e{+}00$
p0	-118.4 ± 2.0
p1	215.6 ± 3.0
p2	-129.2 ± 1.9
p3	43.84 ± 1.73

Figure 61: A fit which will result in a quality factor around 0.5, due to the fact that there are roughly the same signal and background events at the location of the arrow, or invariant mass of the event being considered.
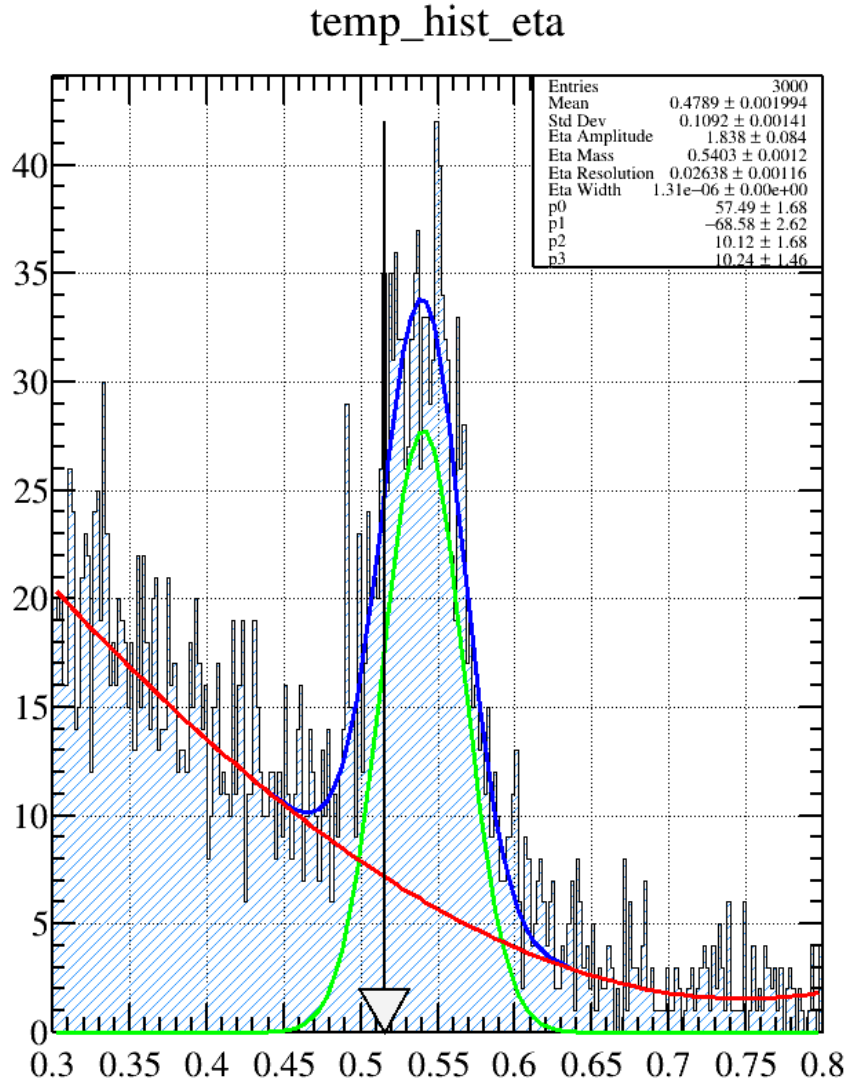
74

temp_hist_eta

Entries	3000
Mean	0.4789 ± 0.001994
Std Dev	0.1092 ± 0.00141
Eta Amplitude	1.838 ± 0.084
Eta Mass	0.5403 ± 0.0012
Eta Resolution	0.02638 ± 0.00116
Eta Width	$1.31e{-}06 \pm 0.00e{+}00$
p0	57.49 ± 1.68
p1	-68.58 ± 2.62
p2	10.12 ± 1.68
p3	10.24 ± 1.46

Figure 62: A fit which will result in a very high quality factor due to the large number signal events in comparison to background events at the location of the arrow, or invariant mass of the event being considered.

4.2.5 Calculating the Quality Factor for $\phi\eta$

Once the fits of the K^+K^- and $\gamma_1\gamma_2$ invariant mass histograms have converged, the final step of calculating a quality factor can be performed. This is done by knowing the signal and background functions, as well as their fitted parameters, for both the K^+K^- and $\gamma_1\gamma_2$ distributions. Knowing the parameters of the fit will allow the user to accurately estimate the number of signal events and the number of background events for a given invariant mass value. The invariant mass value that should be used is the one which corresponds to the event that is being studied, and the parameters are determined by the fit of the invariant mass distribution of nearest neighbors. More specifically, the quality factor associated with the K^+K^- invariant mass distribution will be Equation (7).

$$Q_\phi = \frac{S(m_{K^+K^-})}{S(m_{K^+K^-}) + B(m_{K^+K^-})} \tag{7}$$

In Equation (7), the function S is the convoluted relativistic Breit-Wigner described by Equation (6), and the function B is the convoluted third degree polynomial described jointly by Equation (5) and Equation (3). The equation describes the quality factor solely associated with the K^+K^- invariant mass distribution for one event, and therefore the $m_{K^+K^-}$ variable describes the K^+K^- mass of the event. In addition, the $\gamma_1\gamma_2$ invariant mass distribution will contribute to the total quality factor as well; and it is written in Equation (8).

$$Q_\eta = \frac{S(m_{\gamma_1\gamma_2})}{S(m_{\gamma_1\gamma_2}) + B(m_{\gamma_1\gamma_2})} \tag{8}$$

In Equation (8), the function S is a Voigtian function, which is the convolution of a non-relativistic Breit-Wigner with a Gaussian. The function B is the simply a third degree polynomial. The equation describes the quality factor solely associated with the $\gamma_1\gamma_2$ invariant mass distribution for one event, and therefore the $m_{\gamma_1\gamma_2}$ variable describes the $\gamma_1\gamma_2$ mass of the event. The last, and most important equation ties everything together. In order to study events which contain both a good ϕ candidate, and a good η candidate, one must combine their respective quality factor together in order to obtain a single quality factor for an event. This total quality factor is given in Equation (9).

$$Q_T = Q_\phi * Q_\eta \tag{9}$$

The effectiveness of the quality factor approach is highlighted in Figure [63] and Figure [64]. Each figure contains four sub figures which nicely sum-

marize the results of $1/6^{th}$ of the total $\phi\eta$ data set. Sub figure (a) in both figures is simply the events that are being fed into the analysis and represent what the events would look like if an event weighting of 1 was used for each event. Sub figure (b) in both figures represents the background events which have a weight of $1-Q_T$. One may notice that some of the background events contain what appears to be either ϕ or η resonances inside of them. This is expected to occur in this analysis due to the fact that some ϕ mesons will couple with events that do no contain an η; and similarly, some events with η mesons couple with events that do not contain a ϕ. Upon further inspection, one should also realize that the amplitude of the ϕ or η in the initial events is always greater than the amplitude that exists inside the background events. This suggests that some of the events inside the ϕ or η peak are excellent $\phi\eta$ events.

The third sub figure that exists inside Figure [63] and Figure [64] contain the signal events, or events that are weighted with the value Q_T. One can appreciate that both sub figures contain pure ϕ or η peaks, with absolutely no background. Since the quality factors for each event are saved, they will be used as a weighting every time a histogram is shown in the analysis section. Lastly, the final plot simply shows the sum of the events that are weighted by $1-Q_T$ plus the events that are weighted by Q_T. This will obviously lead to all events having a weight of one, and therefore this histogram is identical to the histogram that is shown in sub figure (a).
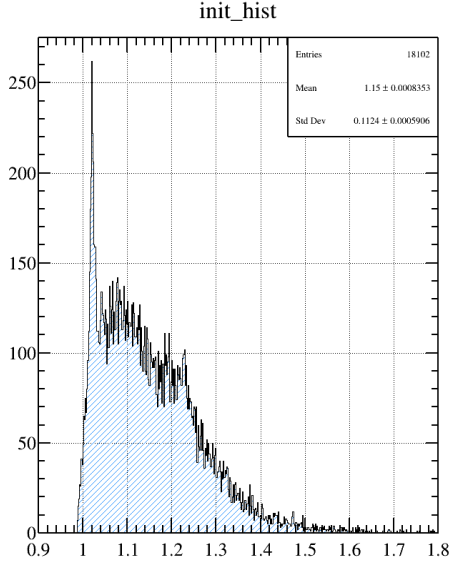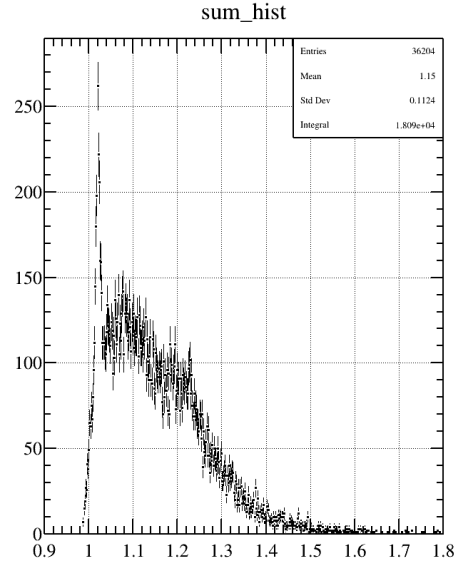
(a) K^+K^- invariant mass distribution over $1/6^{th}$ of the events. All events have a weight of 1, and are therefore a mixture of signal and background.
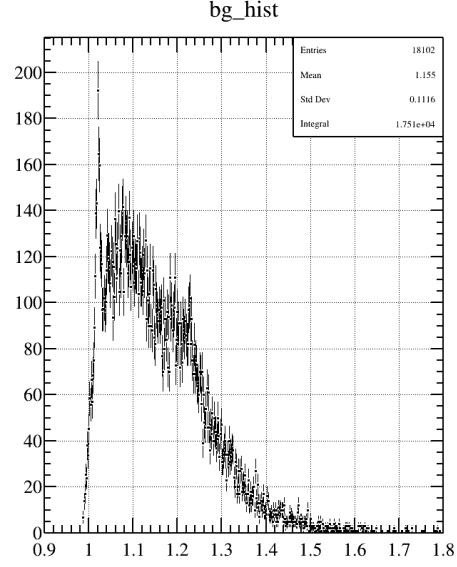
(b) K^+K^- invariant mass distribution over $1/6^{th}$ of the events. All events have a weight of $1 - Q$, and are therefore background.
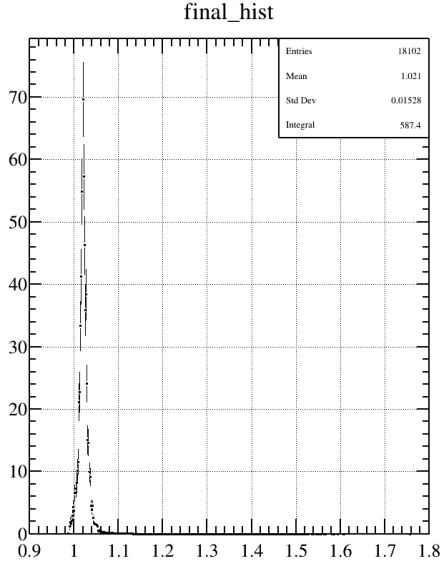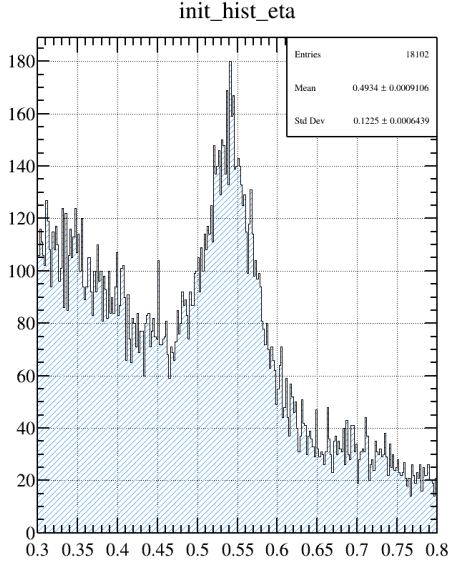
(c) K^+K^- invariant mass distribution over $1/6^{th}$ of the events. All events have a weight of Q, and are therefore signal.
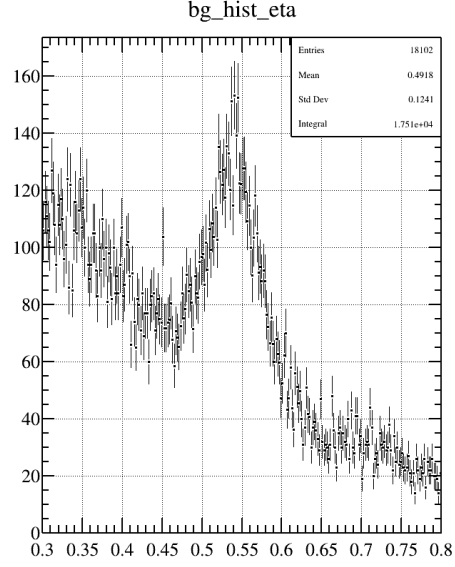
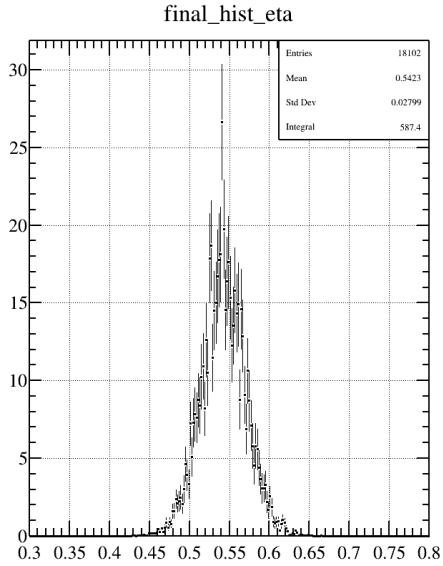(d) The sum of Q plus $1 - Q$ weighted histograms.

Figure 63: Example of how quality factor weighting works over a large statistical sample.

(a) $\gamma_1\gamma_2$ invariant mass distribution over $1/6^{th}$ of the events. All events have a weight of 1, and are therefore a mixture of signal and background.

(b) $\gamma_1\gamma_2$ invariant mass distribution over $1/6^{th}$ of the events. All events have a weight of $1 - Q$, and are therefore background.

(c) $\gamma_1\gamma_2$ invariant mass distribution over $1/6^{th}$ of the events. All events have a weight of Q, and are therefore signal.
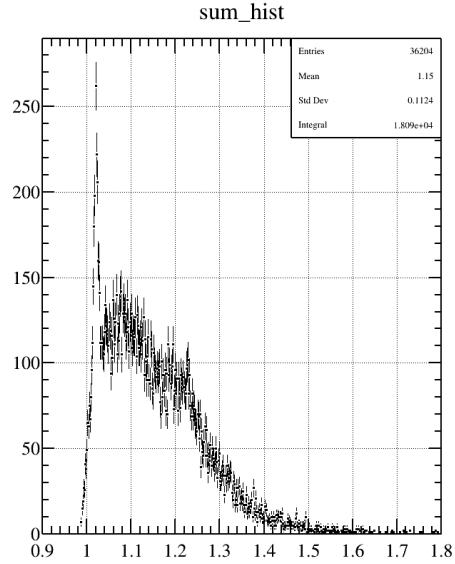
(d) The sum of Q plus $1 - Q$ weighted histograms.

Figure 64: Example of how quality factor weighting works over a large statistical sample.

5 Beam Asymmetry Analysis for $\gamma p \to p\phi\eta$

6 Analysis of $\phi\eta$ Invariant Mass Plot